The Role of Crustal Accretion Variations in Determining Slab Hydration at an Atlantic Subduction Zone

R. W. Allen[1], J. S. Collier[1], T. J. Henstock[2] & The VoiLA Consortium

[1]Department of Earth Sciences and Engineering, Imperial College London, UK

[2]Ocean and Earth Science, National Oceanography Centre Southampton, UK

Corresponding author: Dr. Robert Allen (r.allen16@imperial.ac.uk)

Key Points:

- We identify very low mantle P-wave velocities on the order of 6.5 km s^{-1} in the outer rise region of the Lesser Antilles subduction zone.

- Velocities are the result of two phases of hydrous alteration during accretion at the Mid-Atlantic Ridge and bending at the outer rise.

- Our results imply that water distribution within the slab is heterogeneous on 50-100 km length scales.

Abstract:

We present a 2D P-wave velocity model from the outer rise region of the Lesser Antilles island arc, the first wide-angle seismic study of outer rise processes at an Atlantic subduction zone. The survey consists of 46 OBS receivers over a 174 km profile with velocities resolved to 15 km below top basement. The final velocity model, produced through tomographic inversion, shows a clear decrease in the velocity of the lower crust and upper mantle of the incoming plate as it approaches the trench. We attribute this drop to outer rise bend-related hydration, similar to Pacific cases, but superimposed on spatial variations in hydration generated at the slow-spreading ridge axis. In thin, tectonically controlled crust formed under magma-poor spreading conditions the superposition of these sources of hydration results in compressional velocities as low as 6.5 km s^{-1} beneath the PmP reflector. In contrast, segments of crust interpreted as having formed under magma-rich conditions show velocity reductions and inferred hydrous alteration more like that observed in the Pacific. Hence, variations in the style of crustal accretion, which is observed on 50-100 km length scales both along and across isochrons, is a primary control over the distribution of water within the slab at Atlantic subduction systems. This heterogeneous pattern of water storage within the slab is likely further complicated by along strike variations in outer rise bending, subducting fracture zones and deformation at segment ends and may have important implications for our understanding of long-term patterns of hazard at Atlantic subduction systems.

Plain Language Summary

Subduction zones are locations where one of the Earth's tectonic plates is dragged below the other into the mantle. These are locations of significant seismic and volcanic hazard. Water present in the down-going plate plays an important role in determining the distribution of

these hazards. In well-studied Pacific subduction zones much of this water enters the down-going plate as it is deformed just prior to subduction in a region known as the outer rise. This hydration can be estimated using seismic techniques which measure the time energy takes to travel through the plate, with altered "wet" rocks shown to be anonymously slow. As the structure of the crust in the Pacific is relatively uniform this hydration is evenly distributed. At Atlantic subduction zones such as the Lesser Antilles the structure of the subducting plate is more variable due to a poor magma supply at the ridge where it forms, leading to highly deformed and thinner crust. Our seismic experiment shows the subducting plate is extremely wet, having been exposed to two distinct phases of hydration, one during its formation and another across the outer rise. This may be the root-cause for many of the unusual characteristics of this subduction system.

1) Introduction:

Constraining the volume and distribution of water within subducting oceanic lithosphere is essential to understanding the solid Earth water cycle as well as subduction zone dynamics and associated seismic and volcanic hazards. Pore water within sediments and the upper crust is expelled with compression by a depth of ~40 km (Peacock, 1990). At greater depths water is released from hydrated minerals due to temperature dependent metamorphic reactions within the slab, the most volumetrically significant of which are eclogitization of basaltic crust and the breakdown of serpentinized peridotite (Hacker, 2008; Schmidt & Poli, 1998; van Keken et al., 2011). The release of water alters the physical properties of both the slab and mantle wedge, influencing the distribution of seismicity and melting (Cooper et al., 2020; Kirby et al., 1996; Manea et al., 2014; Peacock, 2001; Schmidt & Poli, 1998; Tsuji et al., 2008). Thermal models commonly predict deserpentinization to be complete by depths of 120 - 150 km, and for many subduction zones, this reaction is the primary source of water release beneath the arc responsible for driving volcanism (Hacker, 2008; Schmidt & Poli, 1998; van Keken et al., 2011).

In the last two decades studies have demonstrated that much of the chemically bound water within the slabs of Pacific and Indian Ocean subduction zones is added just prior to subduction during outer rise bending (Gerya et al., 2021; Grevemeyer et al., 2018; Ranero et al., 2003). This process has been recognised in wide-angle seismic studies by a reduction in V_p within both the lower crust and uppermost mantle from ~50 km outboard of the trench (Grevemeyer et al., 2018 and the references therein) and as a zone of increased conductivity in electromagnetic surveys (Naif et al., 2015). The observations are evidence for extensional deformation of the upper surface of the brittle subducting plate creating faults via which

water can penetrate through to the lower crust and upper kilometres of the mantle (Gerya et al., 2021; Grevemeyer et al., 2018; Ranero et al., 2003).

In the most highly altered cases, at the Nicaragua trench (Van Avendonk et al., 2011) and southern Mariana (Wan et al., 2019) an upper mantle V_p of ~6.8 km s^{-1} may reflect up to 30 % serpentinization (Grevemeyer et al., 2018). Studies at the Chile and Japan/Kuril trench have demonstrated that the extent of outer rise serpentinization depends on several factors. For example, greater hydration occurs where seafloor sediments are thin (Contreras-Reyes et al., 2007), and when the trend of the trench is such that new bend faults are formed (rather than reactivating the pre-existing basement fabric) creating a dense overlapping fault network (Fujie et al., 2018; Shillington et al., 2015). Due to the resolution limitations of most wide-angle studies the depth extent of outer rise serpentinization into the mantle is often poorly constrained, with the best estimates indicating depths on the order of a few kilometres (Contreras-Reyes et al., 2007; Ivandic et al., 2008; Van Avendonk et al., 2011).

What the body of wide-angle studies also demonstrate however is the heavy bias of our current-day understanding of the water cycle at subduction zones towards examples from the Pacific and Indian oceans where lithosphere formed under magmatically robust fast – intermediate spreading conditions is consumed. The structure of slow-spreading oceanic lithosphere forming along the Mid-Atlantic Ridge (MAR) shows clear deviations from the classic 3-layer "Penrose" model (Anonymous, 1972). Here a significant fraction of spreading is magma-poor/amagmatic and accommodated by long-lived high offset detachments, which penetrate the lower crust and upper mantle. This may result in thinning of the crust by several kilometres and complete unroofing of the upper mantle at core complexes, resulting in a much higher volume of water storage within mantle peridotites (Cannat et al., 1995;

Dannowski et al., 2010; Fujiwara et al., 2003; Planert et al., 2010; Smith et al., 2008). For example, sampling of the MAR spreading segment from 22-24° N found that 23 % of the seabed yielded mantle-derived serpentinized ultramafic material (Cannat et al., 1995). More regional studies suggest that 50 % of oceanic lithosphere accreting at the MAR may do so under such a mechanism, and upwards of 70 % in some ridge segments, with the remainder spreading under magmatically-robust conditions to produce crust structurally similar to that of the classic Penrose model produced at intermediate-fast ridges (Escartin et al., 2008).

Unfortunately, a lack of wide-angle studies in mature Atlantic lithosphere (Christeson et al., 2019; Grevemeyer et al., 2018) means that the contribution made to the total subduction water budget at Atlantic subduction zones is poorly constrained. Furthermore, no previous wide-angle studies have investigated outer rise hydration processes at an Atlantic subduction zone, to evaluate to what extent this structurally heterogeneous oceanic lithosphere may undergo further hydration during bending. In this study we present coincident wide-angle, MCS (multi-channel seismic) and MBES (Multi Beam Echo Sounder) bathymetry profiles at the Lesser Antilles subduction zone to investigate these processes.

2) Tectonic Setting:

The survey area lies east of the islands of Guadeloupe and Dominica in the central portion of the Lesser Antilles Arc (LAA), extending from the accretionary prism across the outer rise and onto the incoming plate. The LAA is the result of the subduction of Atlantic oceanic lithosphere beneath the over-riding Caribbean plate (Figure 1) with volcanism along the modern arc initiating from ~25 Ma. Previous wide-angle studies, including those by Christeson et al. (2003), Kopp et al. (2011), Evain et al. (2013) and Laurencin et al. (2018)

have focused on the structure of the forearc and backstop but due to the thickness of the sediment cover and forearc crust, provide few constraints on the velocity structure of the slab. Numerous MCS seismic studies have also been conducted in the region, mainly to investigate the structure of the accretionary prism (Bangs et al., 1990; Laigle et al., 2013; Shipley et al., 1994; Westbrook, 1982). The recent study of Marcaillou et al. (2021) investigated outer rise processes at the oblique, far north-eastern corner of the LAA (located north of Figure 1). Here from MCS imaging tectonically accreted crust was seen to be associated with ridge-ward dipping reflectors extending to a depth of 15 km interpreted as detachments formed during asymmetric spreading that may have been reactivated during outer rise bending. The authors suggest that this weak serpentinized basement likely explains the very low interplate seismic activity associated with the Barbuda-Anegada margin segment above.

The seismic data presented here was acquired as part of the VoiLA Project [Volatile Recycling in the Lesser Antilles, Goes et al. (2019)], with the MCS and wide-angle profiles which form the focus of this study referred to as VoiLA Line 1. Analysis of magnetic anomalies shows that the oceanic lithosphere currently arriving at the trench within our study area formed ~83 Ma [Anomaly C34, Allen et al. (2019), Davy et al. (2020)]. This age is supported by the recovery of Campanian pillow basalts at DSDP site 543 [Figure 1, Biju-Duval et al. (1984)]. The Barracuda Ridge and Tiburon Rise (located north and south of Line 1 respectively, Figure 1) are localised focused deformational features resulting from Quaternary compression along the diffuse North-American/South-American Plate boundary (Patriat et al., 2011; Pichot et al., 2012). While the precise location of the plate boundary is uncertain, according to plate reconstructions our study area straddles the North American/Caribbean plate boundary (Davy et al., 2020). Our profile was located between the

two ridges, in the region labelled the Tiburon Basin in Figure 1 where the influence of this compressional deformation on basement structure is minor (Pichot et al., 2012).

The line is situated in a ~150 km wide spreading segment of the incoming plate between the 15-20 fracture zone (FZ) to the north (age contrast of ~4My) and an unnamed low-offset non-transform offset (NTO) to the south (Figure 1). At the point at which our profile enters the trench these features are both ~100 km distant and so are expected to have little to no influence over the observed structure of the subducting lithosphere. No seafloor spreading discontinuities (FZs or NTOs) are interpreted from gravity or magnetic data to intersect Line 1 itself (Davy et al., 2020; Wessel et al., 2015).
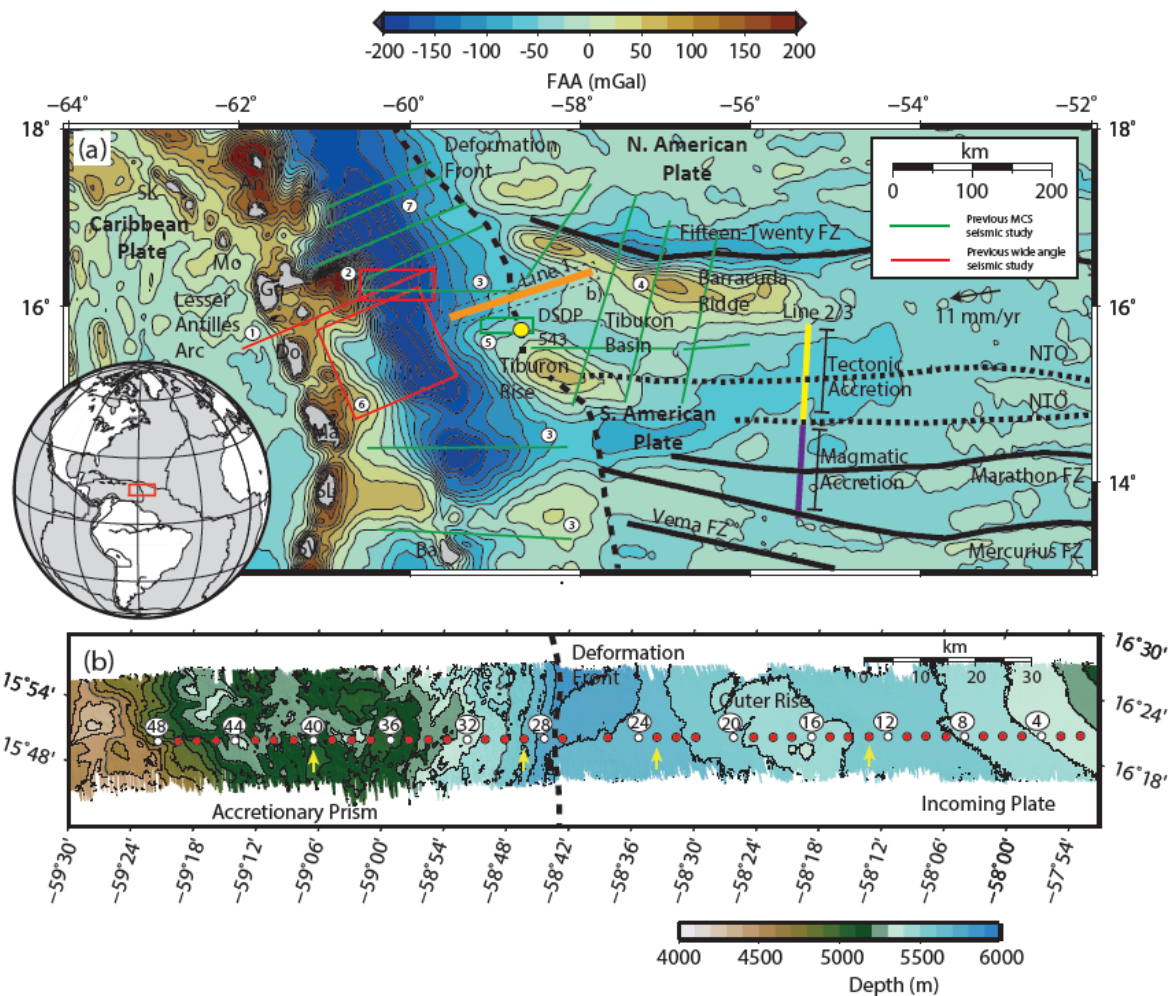
Figure 1: Map of the incoming plate and survey area a) Regional free-air gravity (Sandwell et al., 2014). Line 1, the focus of this study shown in orange. Line 2/3 (Davy et al., 2020) is shown with segments of tectonically accreted crust in yellow and magmatically accreted crust in purple. Black lines show locations of FZs (Fracture Zones, solid) and NTOs (Non-Transform Offsets, dashed) on the incoming plate, from Wessel et al. (2015) and Davy et al. (2020). Other local seismic studies are labelled as follows 1) Kopp et al. (2011), 2) Christeson et al. (2003), 3) Bangs et al. (1990), 4) Pichot et al. (2012), 5) Shipley et al. (1994), 6) Evain et al. (2013), 7) Laigle et al. (2013) b) EM-120 multibeam bathymetry data acquired during JC149 over Line 1 contoured at intervals of 100 m b.s.l.. Circles show OBS locations, every 4th station shown in white for identification only. Dashed line denotes toe of the accretionary prism. Yellow arrows highlight OBS shown in Figure 2. Figures plotted using colour maps of Crameri et al. (2020).

VoiLA Line 2/3 (the focus of a separate study by Davy et al., 2020*),* is ~200 km SE of Line 1 and acts as a calibration for the structure of incoming Atlantic oceanic lithosphere prior to bending (Figure 1). This N-S line crosses 5 distinct ridge segments formed ~65 Ma, separated by NTOs and the Marathon fracture zone. Two diagnostic velocity structures were observed within different segments that were interpreted to represent magmatically robust and tectonically controlled spreading: magmatically-robust segments have a ~2 km thick upper crust and high velocity gradient (1 s^{-1}) above a lower crust ~4.9 km in thickness with a lower velocity gradient (~0.2 s^{-1}), consistent with the structure of magmatic crust formed through fast-intermediate spreading. The lower crust is thinned by 2-3 km within tectonically controlled segments, with velocity inversions indicating the emplacement of highly serpentinized core complexes. Velocities as slow as 7.2 km s^{-1} observed beneath the Moho in such segments indicate extensive hydrous alteration within the incoming plate. The FZs and NTOs themselves do not stand out from the structure of the surrounding crust, but instead have a structure similar to neighbouring segments, consistent with other recent work in the equatorial Atlantic (Growe et al., 2021; Marjanović et al., 2020).

3) Data:

3.1) MCS acquisition and Processing

The data presented here was collected from the research vessel, R.R.S. James Cook in May 2017 (Collier, 2017). Multichannel seismic data was acquired sailing west to east using a 13-gun, 3750 cu in. array towed at a depth of 9 m, with shots every 20 s giving a ~50 m shot separation. Shots were recorded by a 3 km streamer consisting of 240 hydrophones and towed at a depth of 8 m. Following initial geometry assignment and CDP binning (traces assigned to 6.25 m bins), processing consisted of an Ormsby Bandpass Filter (3-8-40-70 Hz), predictive deconvolution (200 ms operator, 100 ms operator prediction distance) and time-dependant amplitude correction (time raised to power correction, time-power constant of 2.3). The final stack uses a velocity structure determined by wide-angle modelling for Kirchoff Pre-Stack Time Migration (PSTM) before depth conversion.

3.2) Wide-angle Acquisition

Wide-angle seismic data was acquired using a 13 gun, 5000 cu in. array, with shots every 60 seconds, resulting in a spacing of ~150 m. Shooting occurred from west to east across a network of 4-component OBS, spaced every ~4 km of which 46 were recovered (Note: OBS1 and OBS25 not recovered). OBS came from two sources, 23 from the German DEPAS OBS pool (broadband instruments) and 25 from the UK OBIC OBS pool, deployed alternately along the profile. Approximately half of the instruments (OBS1-OBS27) were deployed seaward of the toe of the accretionary prism, with the remainder (OBS28-48) deployed on the accretionary prism itself. The OBS recorded continuous data at a frequency of 250 Hz, which were later cut into a 60 s SEGY trace for each shot (Figure 2). On recovery instruments were corrected for internal clock drift and relocated to account for water column drift. The latter used a grid search methodology across local bathymetry, minimizing the misfit with the expected travel time of the water wave arrival along the 2D profile (see Davy et al. 2020). The average resulting correction was 460 m.

3.3) Phase Identification

Arrivals were generally picked from the vertical component of the seismometer which showed the highest data quality. On a few stations on the slope of the accretionary prism, where the seismometer may have struggled to effectively couple with the seabed, the hydrophone component was preferred for picking. All picks used in generating the final V_p model are summarized in Table 1.

The travel time modelling software used required the separation of reflected and refracted arrivals. Phases were identified by forward modelling within the software Rayinvr (Zelt & Smith, 1992). The forward model included the top basement interface picked from the MCS brute stack. Top basement reflections (PbP) were identifiable at offsets of up to 15 km on most seabed instruments (see supplementary Figure S2 for labelled record sections showing picks used to constrain the sediment model). Turning rays in the sediments of the incoming plate outboard of the accretionary prism (profile distances 74-174 km / OBS28-OBS2) were only present as secondary arrivals and were often difficult to distinguish from PbP and the water wave at short offset and hence are only picked on a few OBS. Secondary arrivals within the sediments of the accretionary wedge are clearer, particularly as the sediment column thickens from OBS30 westwards and typically show apparent velocities of less than 2.5 km s^{-1}. Two distinct phases were identified, turning rays within the accretionary prism itself (Psed) and refractions at the decollement interface at longer offsets (Pdec). Reflections from the decollement (PdP) were also picked on most OBS across the accretionary prism, again guided by predicted zero-offset travel times based on interpretations from the MCS. For wide angle modelling reflected phases PbP and PdP were assigned an uncertainty of 0.05s. Psed and Pdec were assigned an uncertainty of 0.1s.
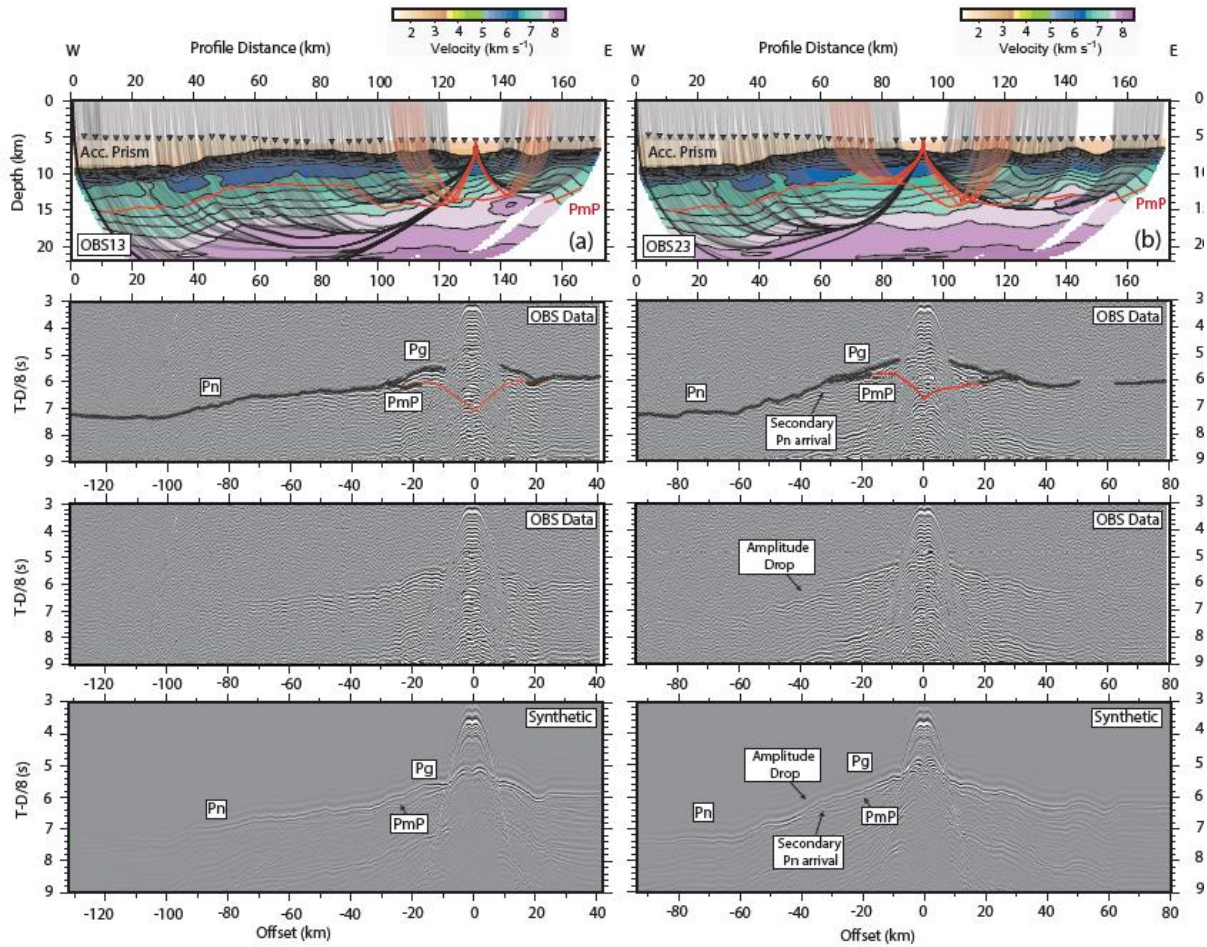
Figure 2: Record section plots for two OBS (13 and 23) located seaward of the prism. Top) Ray trace plots through final V_p model (Section 4.2). First arrival ray paths shown in black, PmP reflections shown in red. Solid red line shows final modelled PmP floating reflector. Middle) Record section plots with and without picks. First arrival picks (Pg + Pn) shown in green, and PmP in red. Red line shows forward modelled PmP travel-times from final velocity model. Bottom) Synthetic record section generated by finite difference modelling of final velocity model. Additional zoomed in images showing the PmP arrival picks in more detail on a larger number of instruments can be found in the supplement (Figure S3)

First arrivals were pickable across the full range of offsets on the majority of OBS outside of

regions of the previous shot wrap around (which particularly obscured the first arrival from

offsets of 80-120 km, Figure 2). Picking through noisy areas was aided by applying a trace

mix to reduced data. Apparent velocities of all first arrivals were highly influenced by the

variable basement topography. First arrival travel times are also greatly delayed where they

pass through the accretionary prism, leading to highly asymmetric arrivals on instruments

such as OBS29 (Figure 2). On instruments west of OBS14, a consistent abrupt drop in the amplitude of the first arrival, often accompanied by an abrupt increase in first arrival travel time, is observed between offsets of 30-40 km (Figure 2).
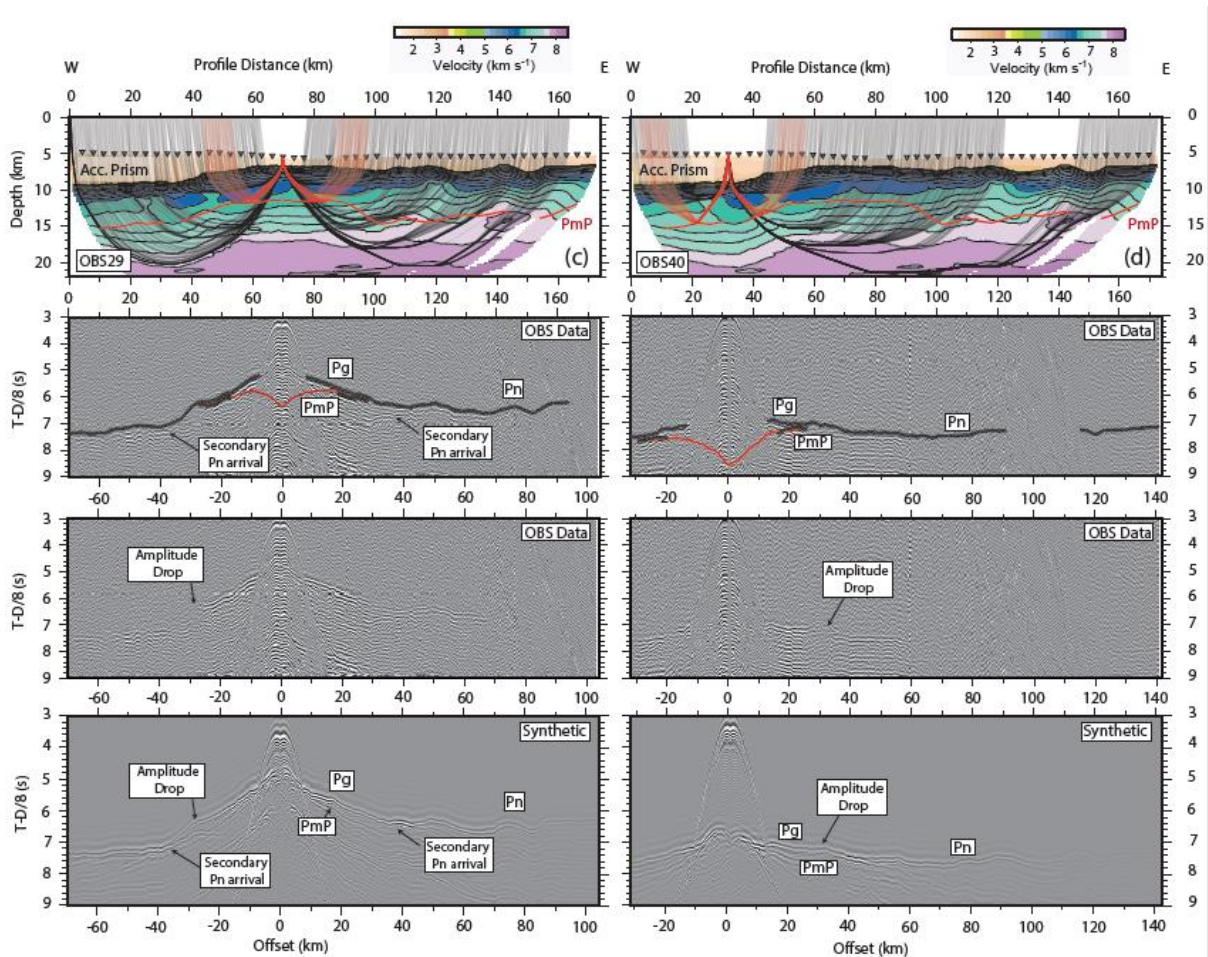

Figure 2 [continued]: Record section plots for two OBS (29 and 40) located on the accretionary prism.

A reflected phase (PmP) was picked at offsets between 20-40 km on most OBS. To the west of OBS14 this reflected phase is less clear, although still identified on all but one of the instruments. A number of OBS also show a strong secondary Pn arrival at ~40 km offset, that may initially be mistaken for a reflection (e.g. OBS29, Figure 2, for more detailed images of PmP picks see supplementary Figure S3). This was shown by the generation of synthetic

seismograms via finite difference modelling to be purely the result of the geometry of the

dipping basement beneath the accretionary prism (Section 4.4).

First arrivals were assigned an uncertainty that increased with offset, with a minimum

uncertainty of 0.05 s at offsets of less than 50 km. Beyond 50 km offset, where the wrap

around noise affects pick clarity, this uncertainty was linearly increased to 0.1 s over a

distance of 25 km. PmP reflections were assigned a constant uncertainty of 0.05 s.

Phase	Phase Type	No. of picks	RMS misfit (s)	Chi-square (χ^2)
Sediment Model (Rayinvr)				
Psed (Incoming Plate)	Turning	723	0.085	0.716
Psed (Accretionary Prism)	Turning	2180	0.090	0.811
PbP (Top Basement)	Reflection	3813	0.049	0.947
PdP (Decollement)	Reflection	676	0.057	1.291
Pdec (Below Decollement)	Turning	424	0.139	1.939
Final Model (Tomo2d)				
PbP	Reflection	3824	0.046	0.85
First Arrivals (Pg/Pn)	Turning	39430	0.053	0.71
PmP	Reflection	4327	0.045	0.82

Table 1: Travel time picks and associated misfits through the Rayinvr sediment model (Zelt & Smith, 1992) and final Tomo2d model (Korenaga et al., 2000) following tomographic inversion. Note that the slight difference in the number of PbP picks used arises due to the different ray tracing algorithms of the two pieces of software, with Rayinvr rejecting 11 picks as it could not find a satisfactory ray path.

4) Modelling

The software used for the final inversion [Tomo2d (Korenaga et al., 2000)] is limited to a

single floating reflector, and hence can only simulate a single reflected phase at a time. As a

result, modelling was done in two stages. An initial sediment model was built in the software

Rayinvr (Zelt and Smith 1992) including constraints from PbP reflections. This model was

then converted into a grid format and used as the lid for a velocity inversion in Tomo2d for

the structure of the crust and upper mantle. Thus PmP was the only reflector to be modelled in the final Tomo2d inversion (see flowchart Figure S4 detailing all inversion stages).

4.1) Sediment Model

The initial sediment model consisted of two layers, separated by the decollement within the accretionary prism beneath a water layer with a constant velocity of 1.5 km s^{-1}. Layers were defined by depth nodes every 500m and velocity nodes every 2 km along the profile. An initial basement surface was generated from picks from the MCS brute stack and converted to depth using semblance velocities. The final sediment model was generated via a process of iterative forward modelling guided where necessary by minor travel time inversions within Rayinvr.

The final model has an RMS travel time misfit of 0.057s (χ^2: 0.760) on the incoming plate (constrained by OBS2-OBS27) and 0.081 s (χ^2: 1.079) within the accretionary prism (constrained by OBS28-OBS48). The greater RMS misfit over the accretionary prism comes from the large number of crossing rays (rays turning in the accretionary prism, Psed, are fitted with an RMS of 0.090s) and the limitation of a single velocity gradient in the layer. Misfits for all picks modelled, are shown in Table 1.

4.2) Tomographic Inversion

Inversion for the structure of the sub-basement crust and upper mantle was performed using the Tomo2d code of Korenaga et al. (2000). The input mesh consisted of velocity nodes every 500 m laterally, with a vertical node spacing of 100 m at the seafloor which increased gradually to a maximum of 500 m at depths of 20 km below the seafloor. The starting model

consists of the pre-determined sediment model from Rayinvr (converted into the appropriate mesh format), above a velocity structure which increases linearly from 4.6 km s^{-1} at top basement to 8 km s^{-1} over 10 km i.e. with no discontinuities initially assumed in the velocity structure associated with the likely depths of the layer 2/3 boundary or Moho. Below 10 km the velocity gradient in the starting model was reduced, with absolute values increasing to 8.2 km s^{-1} at a depth of 30 km below top basement (Figure 3b). A floating reflector was placed at a starting depth of 6 km below top basement to model PmP arrivals in keeping with the approximate depth to the Moho in the region from the study of Davy et al (2020).

An initial lightly-damped inversion step was performed on the sediment model, primarily to ensure that no velocity anomalies were introduced into the mesh by the conversion between the Rayinvr and Tomo2d formats (Figure S4, Step 2). As Tomo2d cannot model secondary arrivals this consisted of the PbP picks only. Following this initial inversion step the PbP arrivals were fitted with an RMS misfit of 0.046s (χ^2: 0.85).

Following testing for parameters that would produce a geologically reasonable model (see text alongside supplementary Figure S4 for further details), regularization parameters were kept constant throughout all steps of the inversion for the sub-basement. Inversion for the sub-basement structure was performed in 2 stages. An initial round of inversion was performed to determine a mean 1D sub-basement velocity model (Figure S4, Steps 3 and 4). This 1D structure was then reinserted into the Tomo2d mesh and used as the starting model for the final inversion stage (Figure 3c). This final inversion was performed in two steps (Figure S4, Steps 5 and 6), firstly to constrain the crustal structure, using all PmP picks and first arrivals with an offset of < 50 km (sufficient to constrain the crustal structure). A second inversion step included all picks, but with the structure more than 1 km above the PmP

reflector damped such that further alterations to the velocity structure would be largely limited to the upper mantle. The final V_p model has an overall RMS misfit of 0.052 s (χ^2: 0.707, Table 1) and is shown in Figures 3a and 4a. For a more detailed breakdown of the inversion workflow and parameterization at each stage see supplementary Figure S4
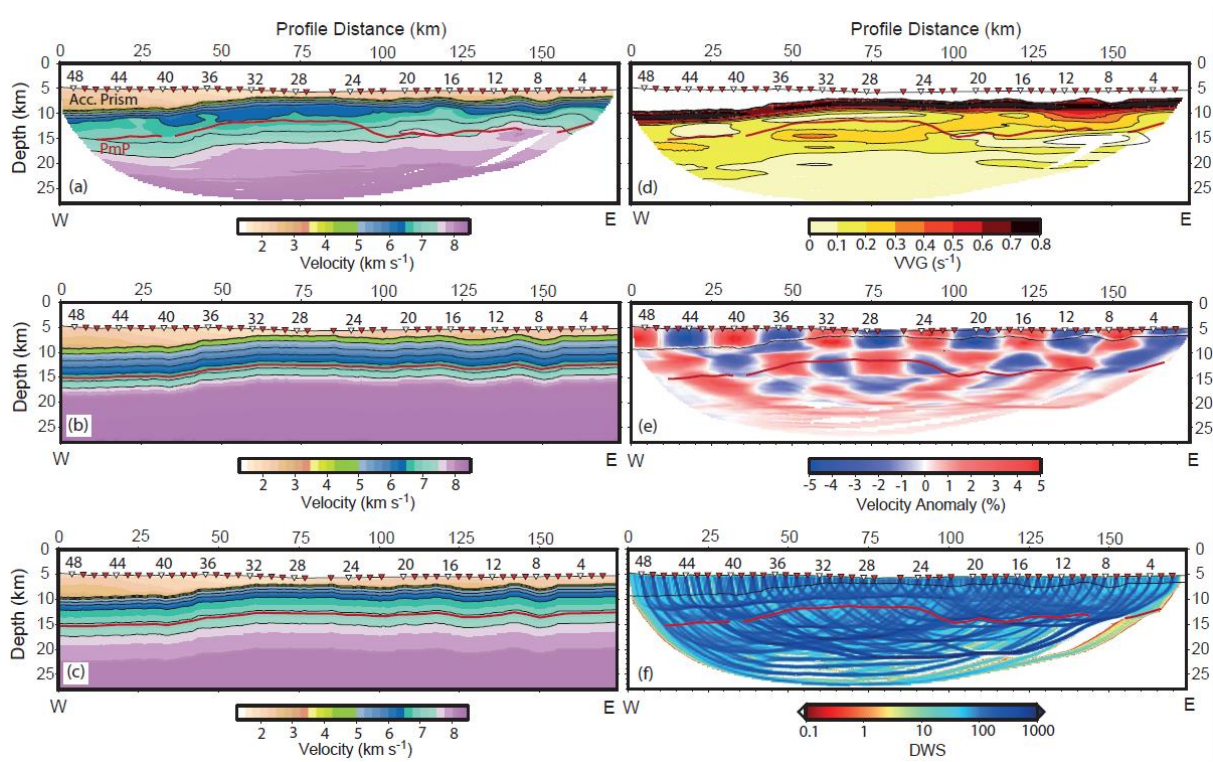

Figure 3: Tomographic inversion results. a) Final V_p profile from Tomo2d. Solid red line shows constrained PmP floating reflector. Triangles show OBS locations, with every 4th instrument highlighted in white. b) Starting velocity model for initial stages of inversion. Solid black line denotes starting PmP floating reflector. c) Self-determined starting model for final stage of inversion (Figure S4). d) Vertical velocity gradient of the final model (excluding sediment layer). A smoothing of 10 x 1 km has been applied. e) Recovery of a 15x5 km checkerboard of 5% velocity anomaly using finalised inversion scheme (Section 4.2). f) Derivative weight sum of ray coverage through final model (Section 4.3).

4.3) Ray Coverage / Resolution

The derivative weight sum (DWS) is an expression of the ray coverage through the final model, a function of the total ray length through each grid cell (Figure 3f). In the eastern part of the model (100-174 km), ray coverage shows a clear concentration of Pn head waves

coincident with the modelled PmP reflector. In the western part of the model (0-100 km), there is a distinct reduction in the concentration of rays turning at lower crustal and upper mantle depths, with many long offset Pn arrivals turning at greater depth. This final ray coverage grid (DWS > 0) is used to mask all plots of the final velocity model, so as only to show regions covered by the data.

The resolution of the final model was analysed using checkerboard testing (Figure 3e). A sinusoidal velocity perturbation of +/-5% was added to the final model and a set of travel times forward modelled through the perturbed model. The full inversion scheme was then re-run using the synthetic travel times as input to recover a new velocity model for comparison against the known input. Note that as many of the secondary arrivals responsible for constraining the sediment structure cannot be modelled in Tomo2d, the sediment section was kept fully damped throughout. Figure 3e shows good recovery of anomalies of 15 x 5 km to depths of as much as 20 km, with some smearing at the ends of the profile. Up to 4.7% of the input 5% anomaly was recovered at depths coincident with the PmP reflector.

4.4) Synthetic Seismograms

In order to confirm that the final inverted velocity model could adequately replicate both travel time and amplitudes from the OBS data, synthetic record sections were generated via finite difference modelling (Figure 2). Synthetic record sections were generated using the visco-elastic finite difference code of Blanch et al. (1993) and Robertsson et al. (1994). As well as the final V_p velocity grid from the wide-angle inversion, geologically reasonable grids for both density and attenuation (Qp) along the profile were also designed. Each was gridded at 20 m intervals (see supplementary Figure S5) with 10 km absorbing boundaries added to the edges and base of the model. The source was modelled as a Ricker wavelet with a central frequency of 8 Hz.

As shown in Figure 2 these final synthetics generally provide an excellent replication of the OBS data, both in terms of travel-times and amplitude. On OBS29 the secondary Pn arrival is clearly replicated at offsets of -20 to -40 km. Furthermore the localised drop in amplitude at ~ 30 km and coincident increase in first arrival travel time is also reproduced in these synthetics on instruments such as OBS23 and OBS29 (Figure 2) without the need for a low velocity layer, or localised attenuation anomaly. The reflected PmP arrival in the synthetic is relatively weak compared to the true record sections due to the smooth velocity increase across the floating PmP reflector in the continuous Tomo2d velocity mesh.
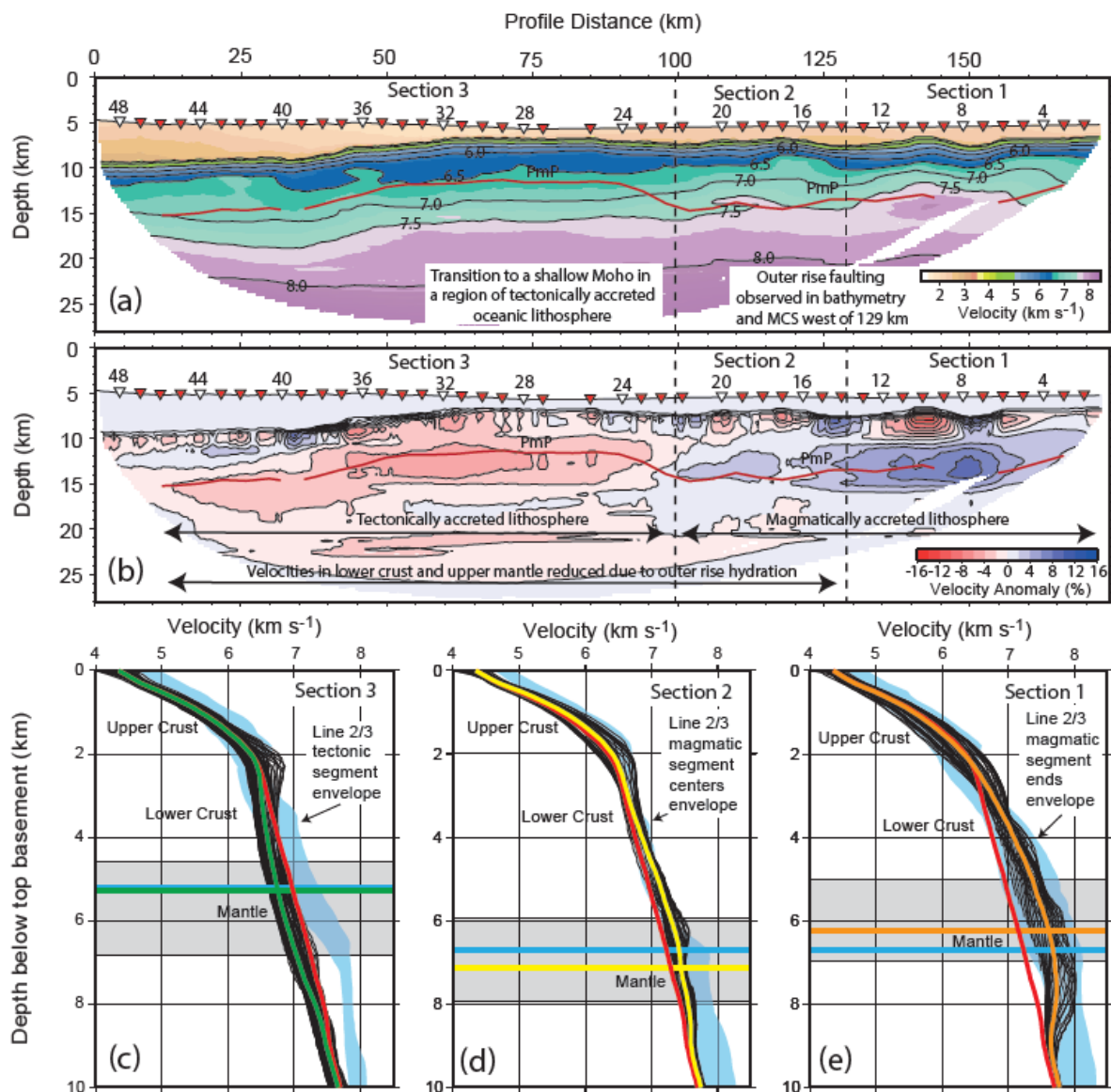
Figure 4: a) Final velocity model with interpretation. We identify 3 distinct sections based on changes in velocity structure and depth of the PmP reflector. Solid red line shows PmP reflector. b) Velocity anomaly plot, computed by subtracting the mean 1D velocity depth profile from the final V_p model. c-e) Comparison of velocity-depth profiles through each of the 3 sections to the results of the calibration line 2/3 from Davy et al. (2020). Thin black lines show the basement velocity structure sampled every 2 km along the profile. Coloured lines (green / yellow / orange) show mean 1D velocity profile within the section. Red line shows mean 1D velocity structure across the whole line (used to create anomaly plot in b). Grey shaded area denotes range of PmP reflector depths in each section, coloured horizontal lines the mean PmP depth. Blue envelopes show the closest fitting velocity structure (magmatic vs tectonic and segment centre vs segment end as marked) from Davy et al. (2020). Blue horizontal line shows the corresponding mean PmP depth from Davy et al. (2020).

5) Results

Figures 3 and 4 shows the final products of the tomographic inversion along line 1. For a more detailed visualisation of the velocity structure within the sediments see supplementary Figure S1. Note that for the presentation of results that follows, the PmP reflector is assumed to represent the petrological Moho boundary between the lower crust and upper mantle, with "crustal thickness" defined as the distance between the top basement and PmP reflector. Alternative interpretations of PmP are discussed in section 6.2.

The structure of the upper oceanic crust (layer 2) across the majority of the profile is found to be ~2 km thick, with velocity increasing from 4.3 km s^{-1} at top basement to 6.3 km s^{-1}, a gradient of 1 s^{-1} (Figure 4). In contrast, the lower part shows distinct variations in thickness, with clear velocity variations in both Layer 3 and the upper mantle along the profile. Based on these variations Line 1 is sub-divided into three structural sections, numbered 1-3 from east to west (Figure 4). The differing velocity structures of these three sections are highlighted in Figure 4b where V$_p$ anomalies below top basement are calculated relative to the mean 1D velocity structure along the entire line. Individual vertical velocity profiles through each of the three sections extracted from the final velocity mesh are plotted in Figures 4c-e. The three-fold variations in the deep velocity structure also coincide with changes in the basement interface structure observed in MCS (Figure 5) and are discussed below.
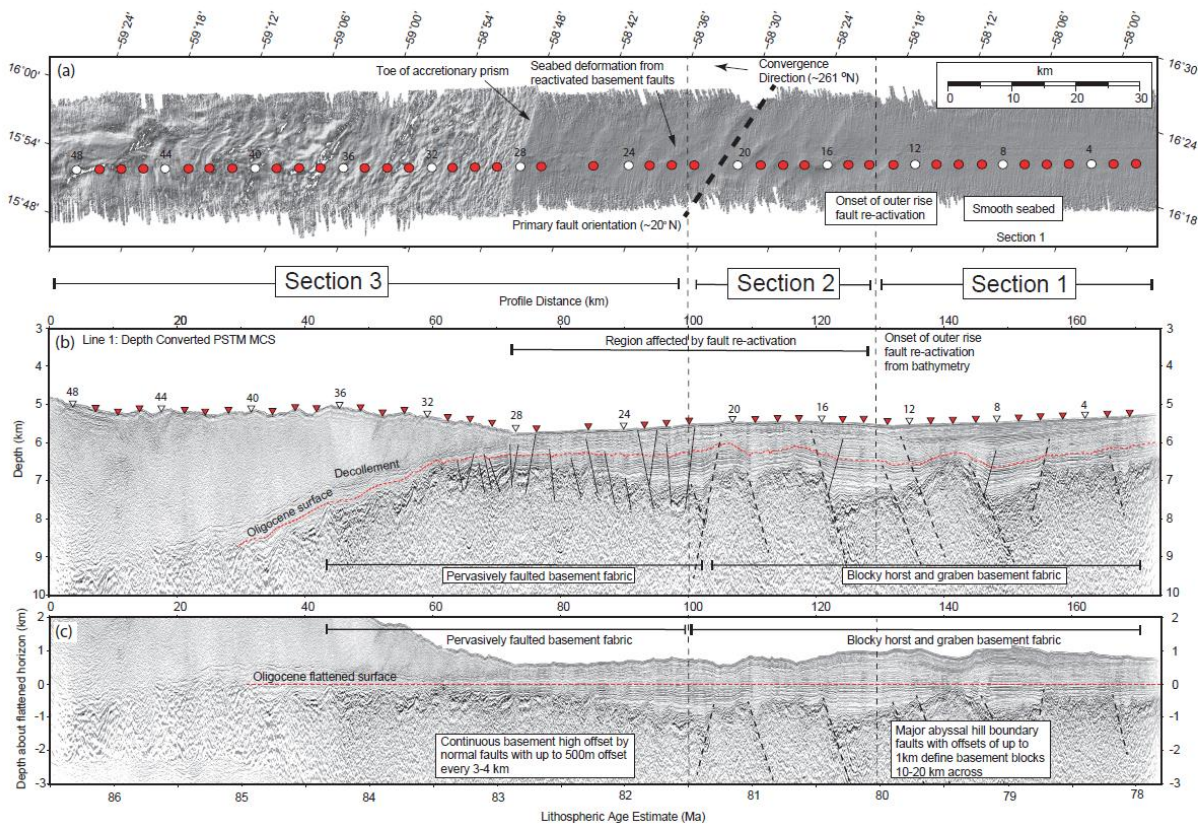
Figure 5: Outer rise structure from MCS and bathymetry data. a) Bathymetry gradient across Line 1. Faulting observed at the seafloor ~50 km from the toe of the accretionary prism, prior to which the seabed is shown to be flat. Faults are dominantly orientated NNE-SSW ~30° from the trench parallel direction. Note the slight line perpendicular grain is a data acquisition artifact. b) Final depth converted PSTM MCS profile. Red dashed line indicates a high amplitude sediment package, interpreted as the upper Oligocene surface. In the east (sections 1 and 2) a blocky basement fabric is defined by half-grabens every 10-20 km separated by normal faults which penetrate deep into the basement with offsets exceeding 1 km. In the west (section 3) the basement is marked by normal faults every 3-4 km and offsets on the order of a few hundred meters across a much more prolonged basement high. The oldest sediments are seen to onlap these basement structures. c) As previous, flattened on Oligocene sediment surface to remove subduction bending and possible younger deformation associated with the uplift of Barracuda and Tiburon ridges. Age estimate assumes that C34n anomaly is currently entering deformation front (Allen et al., 2019; Davy et al., 2020) and a half spreading rate of 20 mmyr^{-1}.

5.1) Section 1

Section 1 (129-174 km profile distance) consists of the easternmost 45 km of the profile. The

basement through this section consists of two half-graben structures controlled by primarily

eastward dipping normal faults every 10-20 km, with throws of 1-1.5 km (Figure 5). These major faults are imaged up to 3 km beneath top basement.

V_p in the lower crust (Layer 3) increases from 6.3 km s^{-1} to ~7.5 km s^{-1} at a depth of 6.2 km beneath top basement coincident with the PmP reflector (a gradient of 0.29 s^{-1}). This velocity gradient is slightly higher than the global-average value of ~0.2 s^{-1} (Christeson et al., 2019; Grevemeyer et al., 2018; White et al., 1992). The lower crust is up to 0.8 km s^{-1} faster than the average of Line 1 (Figure 4B). Crustal thickness in this section varies from 5-6.9 km, though the shallowest depths come from the eastern termination of the profile where velocities are less well resolved (Figure 3E). PmP arrivals are clear throughout the section except for a stretch from 145-155 km. We attribute the absence of pickable reflections here to affects of overlying basement topography rather than any change in the nature of the Moho. Beneath PmP the velocity gradient abruptly falls to < 0.1 s^{-1} within the upper mantle, with velocities of >7.6 km s^{-1} (Figure 3D).

5.2) Section 2

The transition from section 1 to section 2 (at 129 km) coincides with the first observations of outer rise faulting at the seabed (Figure 5a) in bathymetry data. The seabed fabric is oriented ~30 degrees from the trench parallel direction and indicates the reactivation of basement faults with bending across the outer rise. This faulting is also seen in the shallow sediments on the PSTM profile.   The structure of the basement interface in this section is like that of section 1, consisting of 10-20 km scale horst and graben blocks, controlled by high-offset eastward-dipping normal faults.

Across the transition from section 1 to section 2 (at 129 km) there is a reduction in the velocity and velocity gradient in the lower crust and deepening of the PmP reflector to a mean depth of 7.3 km below top basement (Figure 3d, 4b). Velocities across the lower crust increase from 6.3 km s^{-1} to 7.4 km s^{-1}, a gradient of 0.21 s^{-1}. PmP arrivals are again clear throughout the section, with the total crustal thickness varying between 6-8 km. Below PmP the velocity gradient decreases to < 0.1 s^{-1} with V_p as low as 7.4 km s^{-1}.

5.3) Section 3

The transition from section 2 to section 3 occurs at 100 km. At this point there is a clear transition in basement structure to a prolonged high (extending for at least 60 km) punctuated by more tightly spaced normal faults every 3-4 km, with throws at top basement up to a maximum of 500 m. In Figure 5c, basement structure is restored (removing the effect of bending into the trench) by flattening on a high amplitude sediment interval pickable across the majority of the MCS profile. This horizon is interpreted as the top Oligocene based on the seismic facies description of Pichot et al. (2012), though we lack well control to corroborate that interpretation and would also pre-date any local deformation associated with the uplift of the Barracuda Ridge or Tiburon Rise (Patriat et al., 2011; Pichot et al., 2012).

The transition from section 2 to 3 coincides with a reduction in crustal thickness to a mean of 5.3 km, with the PmP reflector shallowing by 2 km over a distance of 5-10 km. A reduction in the velocity of the lower crust and upper mantle is also observed with lower crustal velocities increasing from 6.3 km s^{-1} at the top of layer 3 to 6.5-6.7 km s^{-1} at the PmP interface. The velocity gradient in the lower crust here is < 0.1 s^{-1}, less than half that observed in sections 1 and 2.

Velocities within the upper mantle range from 6.5-6.7 km s^{-1}. In contrast to the remainder of the profile, the vertical velocity gradient increases abruptly beneath the PmP reflector to 0.3 s^{-1} (Figure 3D). This increased gradient drops off over a depth interval of 3-4 km, to a more typical upper mantle velocity gradient of < 0.1 s^{-1}. Velocities at the PmP interface are 6-8 % slower than the rest of the profile at the same depth (Figure 4B). This slow anomaly extends to ~10 km beneath top basement.

6) Discussion

6.1) Crustal Accretion Variations

VoiLA line 2/3 (Davy et al., 2020) allowed us to investigate variations in Atlantic crustal accretion style along an isochron. Here we can investigate similar variations across an ~8 My time interval. Clear changes in basement structure, V_p, and the depth of the PmP reflector are observed along Line 1. We interpret these variations as a product of structure inherited from accretion at the MAR, overlain by secondary deformation and hydration as the incoming plate bends through the outer rise.

As shown by Davy et al., (2020) the accretionary structure is expected to have two forms – magmatically robust and tectonically controlled – both of which are moderated slightly towards segment ends. Along calibration line 2/3, crust formed under magmatically-robust spreading conditions showed a typical "Penrose" structure, with an average thickness of 6.7 km. Segments of thinned crust with a mean thickness of 5.2 km were interpreted as having accreted under magma-poor conditions by tectonically controlled extension. The latter was supported by slow upper mantle velocities (as low as 7.2 kms^{-1}), indicative of hydration and the identification of several core complexes as velocity inversions in the upper crust. The

results of this study are compared to the velocity structures of the three interpreted sections of Line 1 in Figure 4C-E.

Sections 1 and 2 of Line 1 closely resemble the magmatically robust crustal segments of Line 2/3, in both thickness and velocity structure (Figure 4c). Section 2, with a crustal thickness of 7.3 km and a well-defined transition between layer 2 and 3 is therefore a good match to the velocity structure of oceanic crust formed globally through magmatically robust spreading, along fast/intermediate spreading ridges such as in the Pacific (Christeson et al., 2019; Grevemeyer et al., 2018; White et al., 1992). The crust of section 2 is up to 1 km thicker, with lower crustal velocities 0.2-0.3 km s^{-1} slower than in section 1. The onset of outer rise faulting is the simplest explanation for the decrease in velocity of the lower crust between sections 1 and 2, which coincides with the onset of the outer rise high observed in our MBES data (Figure 1b). Pichot et al. (2012) interpreted the flexural bulge at the same location from gravity data. By comparing the velocity structures from the two VoiLA profiles (Figure 4), we find section 1 (which lies closest to the 15-20 FZ) strongly correlates with the structure of the ends of magmatically robust spreading segments observed on line 2/3, and section 2 as from a central portion of the segment where melt is more focused. Modest crustal thinning towards the segment ends is consistent with trends observed both within the magmatic spreading segments of Line 2/3 and studies of crustal thickness trends within magmatic segments at the MAR (Growe et al., 2021; Lin & Phipps-Morgan, 1992; Lin et al., 1990; Marjanović et al., 2020; Wang et al., 2015). The interpreted boundary between sections 1 and 2 occurs ~ 75 km from the mapped 15-20 FZ, which is further than any of the segment ends in the Line 2/3 survey area, but both the segment width and FZ offsets are significantly larger than observed in the Davy et al. (2020) study.

In section 3, the PmP reflector shallows to 5.3 km beneath top basement indicating that west of 100 km the profile transitions from a region of magmatically robust crust to a thin, tectonically controlled crust. Crustal thinning on the order of several kilometres occurs due to asymmetric rifting associated with amagmatic spreading (Dannowski et al., 2010; Planert et al., 2010). Within section 3 this thinning is entirely accommodated in the lower crust (Figure 4). The depth of the PmP interface here is an excellent match to that observed by Davy et al. (2020) in crust of similar affinity (Figure 4C), though V_p of the lower crust is as much as 0.5 kms^{-1} slower.

Magmatically robust spreading is generally associated with a smooth basement fabric, with long, narrow and low elevation abyssal hills (Escartin et al., 2008). However, due to slow-intermediate spreading rates, abyssal hills within the Atlantic are generally broader in the ridge perpendicular direction and show greater deviation from the mean basement depth than their Pacific equivalents (Goff, 1991; Goff et al., 1993; Goff et al., 1995; Macario et al., 1994; Roth et al., 2019). Abyssal hills formed under slow spreading conditions are often observed to be highly asymmetric and inward facing (towards the ridge), as seen in the half-graben geometry of the basement of sections 1 and 2, (Goff et al., 1995; Roth et al., 2019). The basement topography within the magmatically robust sections of Line 1 has an RMS variation relative to the mean basement depth along the profile of 276 m (Note: this calculation was done using the flattened section in Figure 5C, to remove any deformation associated with plate bending as much as possible). This is consistent with abyssal hill geometry measured by Goff (1991) at several test sites along the MAR with RMS abyssal hill relief of up to 299 m,. This basement topography is therefore consistent with abyssal hill structures formed under slow spreading conditions elsewhere in the Atlantic and is not at odds with the magmatically robust velocity structure beneath.

The thin, tectonically controlled crust of section 3 shows a smoother basement profile with comparatively limited fault throw on the order of 100s of meters. Within regions of asymmetric spreading, the crust on the conjugate side of the ridge (i.e. the upper plate) to the primary detachment can still display a significantly thinned layer 3, whilst lacking the high offset detachment faults and exhumed core complexes commonly associated with such spreading (Planert et al., 2010). The top basement in section 3 is elevated with a thin overlying sediment column compared to that from sections 1 and 2, as demonstrated by the onlap of the pre-Oligocene sediments between 74-100 km, (Figure 5c). Non-isostatic, stress-supported topography during accretion is another clear indicator of asymmetric spreading and further supports our interpretation of section 3 (Wang et al., 2015). Our failure to image either deep detachment faults or outer rise bend faults to any great depth within the crust may be purely a function of the source size and streamer length of the survey (5000 cu in. and 3 km respectively) and should not be misinterpreted as the total absence of deep penetrating faults in this area. Marcaillou et al. (2021) clearly image detachment faults in crust of similar affinity to a depth of 15 km below top basement within the incoming plate along the north-east corner of the arc but with a 6500 cu in. source and 4.5 km streamer.

The transition from magmatically robust crust to tectonically accreted material represents a temporal shift in magmatism at the ridge. We believe that this is the first time that such a transition has been clearly captured in a wide-angle survey in mature oceanic crust away from the MAR. Wang et al. (2015) identified long term variations in crustal thickness tied to magma production rates on a time scale of >10 My in a segment of the MAR at 28°N (equivalent to every ~200 km at Atlantic slow-spreading rates), though Tucholke and Lin

(1994) suggest that flips between symmetric and asymmetric spreading could occur on shorter timescales of as little as 2 My. At the other end of the scale Vaddineni et al. (2021) observe 27 My of continuous magmatically robust accretion from an along flow-line wide-angle study adjacent to the Charcot FZ in the Equatorial Atlantic. Our observations support a period of magmatically robust accretion to form sections 1 and 2 lasting a minimum of 3.75 My and at least 5 My of tectonically controlled spreading across section 3 (with assumed spreading half-rates of 20 mm yr^{-1}).

6.2) Extent and origin of hydration

Comparison with the different types of accretionary structures found along Line 2/3 allows estimating the level of hydration as the lithosphere enters the outer rise and how much additional hydration occurs during outer rise bending. The consistent velocity structure of the 2 km thick oceanic layer 2 across the entire line indicates that the upper crust is not greatly affected by secondary deformation and water penetration across the outer rise. Whether this is the result of pre-existing extensive hydrothermal alteration (Christeson et al., 2019), or the relative insensitivity of the velocity of basalt/diabase to hydration (Hacker et al., 2003) is unclear.

Across sections 1 and 2 of the profile, where the PmP reflector is at ~6.5 km depth and coincides with velocities on the order of 7.5-7.7 km s^{-1} in the upper mantle, we are confident in our interpretation of this reflector as the Moho. In section 3, where the PmP reflector shallows to 5.3 km beneath top basement, this interpretation is less clear cut. In areas of magma-poor spreading, mixed lower crustal compositions are expected due to the absence of a long-term stable magma chamber and detachment faulting that can emplace mantle rocks at

shallow depth (Cannat, 1993; Sleep & Barth, 1997), while the V_p of gabbros and partially serpentinized overlaps peridotites at around 7 km s^{-1} (White et al., 2010).

In our final model anomalously slow velocities extending to depths of up to 10 km beneath top basement strongly support an interpretation of high levels of alteration up to 4 km beneath PmP (Figure 4B). Yet we are still able to constrain this reflector with picks from all bar one of the OBS. At the same time, we observe an abrupt increase in the velocity gradient beneath the PmP reflector in this section. It is extremely difficult to reconcile these observations as a consequence of hydration alone and must surely indicate some corresponding lithological change which is still preserved as an acoustic impedance contrast despite the overlying hydrous alteration and deformation. At these depths this is almost certainly the petrological Moho discontinuity.

Figure 6 shows the upper mantle V_p anomaly along the incoming plate as it approaches the trench compared to a number of Pacific examples from Grevemeyer et al. (2018). Velocities in the upper mantle immediately beneath PmP decrease by 0.4 km s^{-1}, across the 29 km width of section 2. This length scale and degree of alteration is like that observed in wide-angle studies in the Pacific where the incoming plate consists entirely of magmatically robust oceanic lithosphere and clearly corresponds with the onset of outer rise bend faulting at the boundary between sections 1 and 2.

The observed reduction in velocity of the lower crust and upper mantle across section 3 are indicative of a very high level of hydration within the lithosphere currently beneath the outer rise. Velocities in the thinned crust of layer 3 here are up to 0.5 km s^{-1} slower than Line 2/3 (Figure 4b). A velocity reduction through hydration alone on this order would require a

typical MAR gabbro to undergo almost total (100 %) alteration to amphibolite facies, or the presences of a significant olivine rich component to promote the formation of low velocity serpentine. Alternatively, the observed velocity reduction could be explained by the serpentinization of crust with 15–30 vol % antigorite content (Hacker et al., 2003), which would again be consistent with the magma-poor origins of this section of the crust.
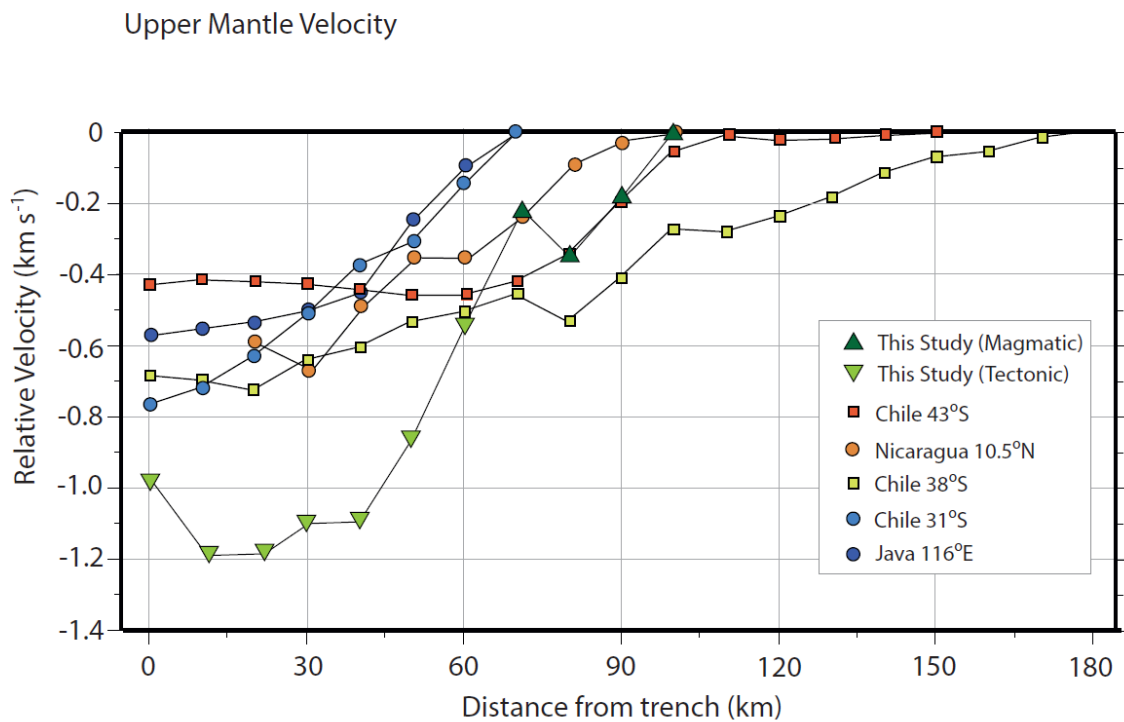
Upper Mantle Velocity

Figure 6: Variations in upper mantle velocity with distance from trench adapted from Grevemeyer et al. (2018). Velocities are relative to maximum upper mantle velocity immediately below PmP along the given profile. Note that across sections 1 and 2 of Line 1 where accretion is magmatic, velocities show a similar rate of decrease with distance from the trench to intermediate-fast spreading lithosphere at Pacific subduction zones. The transition to section 3, and tectonically accreted lithosphere shows a very abrupt reduction in upper mantle velocity, with the upper mantle consistently 0.5 kms^{-1} slower than the Pacific examples. We interpret this difference to be primarily the result of pre-existing hydration of the tectonically accreted lithosphere during formation. Note that for the purposes of this plot distance from the trench is measured eastward from the 45 km mark along Line 1. West of this point the accretionary prism reaches almost full thickness, and we assume that this layer prevents any further hydration.

Velocities of 6.5-6.7 km s^{-1} within the upper mantle of the outer rise would, as far as we are aware, represent the most significant hydration anomaly observed at the point of subduction anywhere globally (Figure 6). Using the linear relationship between mantle velocity and

serpentinization established by Grevemeyer et al. (2018), this would be equivalent to as much as 45-50 % serpentinization at the mantle interface (approx. 6-7 wt % H_2O). The high velocity gradient (~0.3 s^{-1}) observed beneath PmP in section 3 (Figure 4D) is interpreted as a steady decrease in the degree of serpentinization over a depth window of ~4 km within the upper mantle. Assuming a decrease to 0 % serpentine at the depth of the 7.75 km s^{-1} contour (10 km below top basement) this would mean an average of ~25% serpentinization across the upper 4-5 km of the mantle. Although the proposed maximum degree of serpentinization is higher than observed by previous wide-angle studies, this depth extent is similar (Contreras-Reyes et al., 2008; Ivandic et al., 2008; Van Avendonk et al., 2011).

At the Chile trench Contreras-Reyes et al. (2007) demonstrated that hydration in the outer rise is influenced by the thickness of the sediment blanket on the incoming plate, with the greatest V_p reduction coincident with exposed basement at the seabed. Studies of the Japan-Kuril system have also shown that outer rise hydration is increased where fresh bend faults form parallel to the trench, rather than bending accommodated by reactivation of a pre-existing basement fault fabric (Fujie et al., 2018). Yet, at the Lesser Antilles these very high levels of hydration are observed within the incoming plate despite a sediment blanket that exceeds 1-2 km, and a fabric of reactivated basement faults of very low offset throughout much of the sediment column (Figure 5), indicating that either there is something fundamentally different about the mechanism of outer rise hydration in the Atlantic (e.g. due to very slow convergence rates at the trench), or most likely an amount of hydrous alteration is inherited from prior to the outer rise. Given the distance to the nearest mapped FZs and NTOs (Figure 1) we can also rule these out as a means of facilitating deep hydration along our profile.

Along the calibration line, Davy et al., (2020) observed velocities as low as 7.2 km s^{-1} at the upper mantle in equivalent, tectonically controlled crust prior to arriving at the outer rise. The most likely scenario is therefore that much of the hydration observed in section 3 is inherited from prior to plate bending and is tied to the mode of crustal accretion. We observe a rapid decrease in the velocities of the upper mantle across an ~10 km distance coincident with the transition from magmatically accreted crust in section 2, to tectonically accreted lithosphere in segment 3 (Figure 7). The rate at which hydration increases (i.e. upper mantle velocity decreases) across this transition, far exceeds that observed in section 2, or at any previous study. Thin, highly tectonised lithosphere can promote deep hydrous alteration as the crust is accreting (Minshull et al., 1998). While the largest mapped faults are observed at the eastern end of the profile, section 3 also contains a dense fault network. Assuming a similar pre-existing level of hydration to Line 2/3 in this case, this would imply a further velocity reduction of 0.5-0.7 km s^{-1}, equivalent to a further ~16 % serpentinization of the upper mantle due to bending across the outer rise, much more in keeping with the existing body of studies (Grevemeyer et al., 2018 and the references therein). The style of accretion at the ridge is thus a primary influence over total hydration of the incoming plate both at the MAR and across the outer rise and an extremely important control over the distribution of water within the slab.

6.3) Implications for slab hydration at the Lesser Antilles subduction zone

Estimates from mapping at the MAR ridge suggest that anywhere from 30-70 % of the accreting lithosphere may be doing so via amagmatic spreading (Cannat et al., 1995; Escartin et al., 2008). Changes between dominantly magmatically robust and magmatically limited accretion occur between spreading segments, often on a length scale of 50-100 km in the

ridge parallel direction, and on a timescale on the order of 2-10 My in the spreading direction (Escartin et al., 2008; Tucholke & Lin, 1994; Wang et al., 2015). Our work shows that these variations in spreading mechanism at the ridge appear to be an important control over slab hydration in the Atlantic. Based on our results tectonically accreted sections of the oceanic lithosphere may carry up to twice as much water in the form of serpentine in the upper mantle compared to more magmatic segments of the ridge, due to the deep circulation of water through the thinner, tectonized crust both during accretion, and again across the outer rise leading to a highly spatially and temporally varying water flux into the arc.

In the Pacific, outer rise hydration is the most significant contributor of water to the slab mantle, varying with sediment thickness and structural trends in the fairly homogenous intermediate-fast spreading lithosphere that constitutes the majority of slabs (Contreras-Reyes et al., 2007; Fujie et al., 2018). Along the southern LAA, the Barbados accretionary prism spills out onto the incoming plate and sediment thickness reaches up to 7 km due to the large sediment supply from the South American continent with the Tiburon Rise acting as a barrier to northward sediment transport (Biju-Duval et al., 1982; Moore et al., 1998). It is therefore reasonable to also expect an overlapping long wavelength trend with greater outer rise hydration north of the Marathon and Mercurius fracture zones compared to the extremely sediment-rich trench of the southern arc.

It has been proposed that increased rates of Wadati-Benioff seismicity and arc magmatism, as well as thicker arc crust in the centre of the LAA beneath Guadeloupe and Dominica can be tied to prolonged periods of enhanced water release from the subducting 15-20, Marathon and Mercurius FZs (Cooper et al., 2020; Paulatto et al., 2017; Schlaphorst et al., 2016), as well as a now largely subducted rifted boundary between the Atlantic and older Proto-Caribbean

oceanic lithosphere which lies immediately south of the Mercurius FZ at today's trench (Bie et al., 2022; Braszus et al., 2021; Cooper et al., 2020). Cooper et al. (2020) observed Boron anomalies in the magmas of the islands of the central arc characteristic of a large contribution of fluids from the breakdown of serpentine.

Recent wide-angle studies from the Atlantic, have found the structure (and thus degree of alteration) at FZs to be highly dependent on the mechanism of crustal accretion in the adjacent ridge segments. Studies at the Marathon (Davy et al., 2020), St. Paul (Growe et al., 2021) and Chain (Marjanović et al., 2020) FZs, flanked by magmatically robust ridge segments found little structural variation and little indication of elevated hydration, while at the Romanche transform fault, flanked to the south by a tectonically accreting ridge segment Gregory et al. (2021) observed up to 30% serpentinization of the upper mantle (and potentially up to 80% within the fault zone itself). Thus, FZs may also represent a highly varying hydration anomaly along the slab on 2-10 My timescales in keeping with changes in the accretionary fabric of the adjacent crust. This may have a more significant impact on the 1st order structure of such discontinuities than parameters such as age contrast or geometry (Davy et al., 2020).
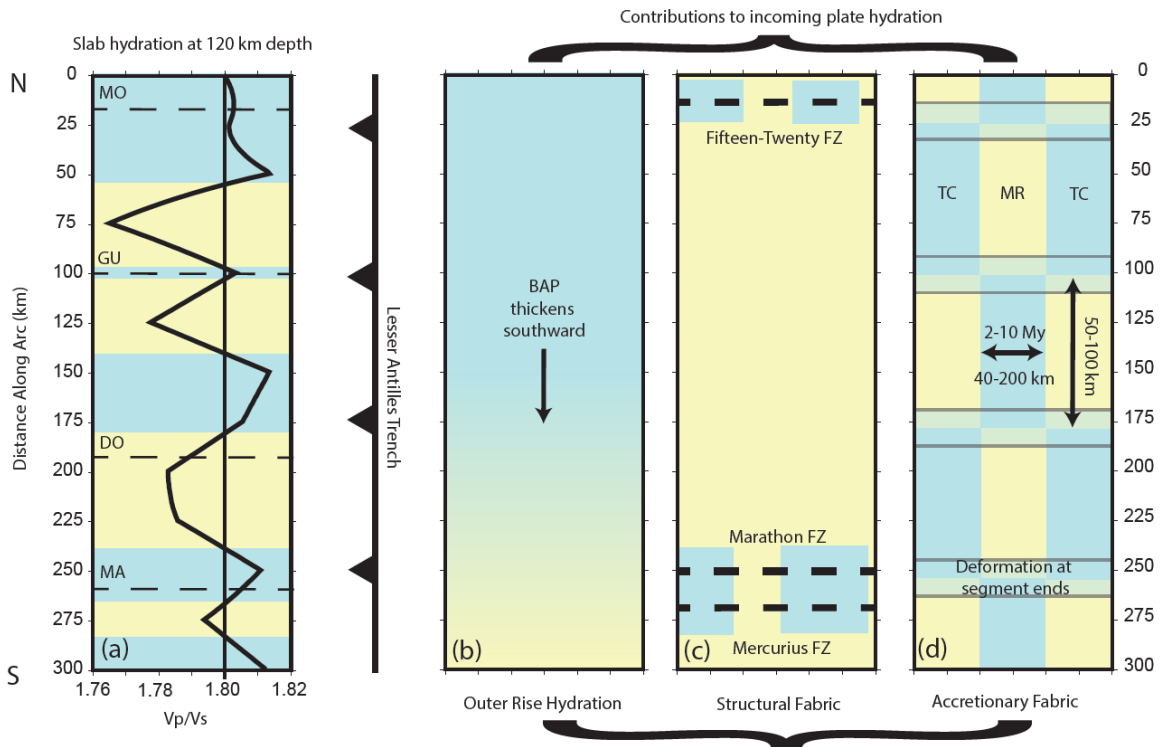
Figure 7: Schematic showing 3 key contributors to slab hydration at the Lesser Antilles arc, where blue shading indicates more hydration and yellow less. a) Observed V_p/V_s ratio above the slab at a depth of 120 km beneath the arc (the deserpentinization depth) from the study of Bie et al. (2022). A V_p/V_s ratio of 1.8 is equivalent to approx. 10 % serpentinization (White et al., 2010). Variations in hydration on the 50 to 75 km length scale are a good indicator of the contribution of variations in accretion to the total water content of the slab. Mo-Montserrat, Gu=Guadeloupe, Do=Dominica, Ma=Martinique. b-d) Predictions of incoming plate hydration based on our study and those from other subduction zones. b) Probable long wavelength variations in outer rise hydration due to thick sediments of the BAP to the south. c) Variable hydration along subducting fracture zones. A rifted boundary between the Proto-Caribbean and Atlantic spreading domains south of the Mercurius fracture zone may also represent a focused hydration anomaly (Braszus et al., 2021; Cooper et al., 2020). d) Variations in accretionary fabric (i.e. magmatically robust, MR vs tectonically controlled, TC accretion) are likely to occur along strike on length scales of 50-100 km, between ridge discontinuities and 2-10 My timescales in the ridge perpendicular direction.

The distribution of water within Atlantic slabs is thus a function of three factors, accretionary fabric, subducting FZs (and other large-scale plate fabric), and outer rise hydration trends. Each of these varies on different length scales along the subduction front, contributing to a highly heterogeneous distribution of chemically bound water within the crust and upper mantle of the slab. In Figure 7 we compare the typical length scales of these proposed

influences over slab hydration to V_p/V_s in the mantle below the LAA from the tomography of Bie et al. (2022). They observe distinct V_p/V_s anomalies above the slab at ~120 km depth (the expected de-serpentinization depth under this system), due to water release into the sub arc mantle. These hydration anomalies vary primarily at a length scale of 50-100 km, in keeping with the proposed wavelength of variations arising from lateral changes in accretionary fabric within the slab.

While we do not dispute the potential role of fracture zones in dictating patterns of arc behaviour at the LAA, the very high levels of hydration observed in this study would suggest that focused hydration of regions of tectonised oceanic lithosphere must also play an important role. Instead we believe that 2000-20000 km^2 patches (measuring 50-100 km along strike and 40-200 km across strike, see Figure 7) of tectonically controlled lithosphere are likely responsible for the bulk of water delivered to sub-arc depths beneath the LAA. This pattern of slab dehydration will correspond to variations in mantle wedge melting on similar length scales. Therefore, magmatic output along the island arc (Cooper et al., 2020) and dehydration embrittlement driven intra-slab seismicity (such as the damaging 2007 Mw7.4 Martinique earthquake (Yamasaki & Seno, 2003) will reflect these temporal and spatial hydration variations within the slab. Similarly complex patterns of slab hydration should be expected at the Scotia arc which also subducts slow-spreading Atlantic lithosphere.

7) Conclusions

Here we have presented the first *P*-wave velocity model across the outer rise and accretionary prism of the Lesser Antilles subduction zone. Our key findings are as follows:

- Distinct variations in the velocity structure of the crust and upper mantle are observed along the profile. These are interpreted as a combination of variations in accretion style at the Mid Atlantic Ridge plus deformation and hydration as the lithosphere passes over the outer rise. The duration of magma-rich and magma-poor accretion episodes at the ridge axis is at least 3-5 My.

- Observations of upper mantle V_p beneath the outer rise as low 6.5 kms^{-1} are indicative of much higher levels of serpentinization (up to 50%) than has been observed in previous studies of Pacific and Indian Ocean subduction systems. This is likely due to the lithological heterogeneity and pre-existing deep hydration of tectonised lithosphere during accretion at the ridge. More magmatically robust regions of Atlantic oceanic crust do not appear to be significantly more affected by outer rise hydration than intermediate-fast spreading Pacific examples.

- The distribution of tectonically accreted lithosphere throughout the Atlantic in combination with focused hydration at fracture zones and NTOs, and the contribution from outer rise hydration leads to a water distribution within the Lesser Antilles slab which is both more hydrated, and more spatially heterogeneous than would be expected from an equivalent system subducting crust produced by intermediate to fast spreading.

- Due to the very high levels of hydration proposed, water stored in patches of tectonically accreted lithosphere may be the single largest contributor to water released beneath the Lesser-Antilles sub-arc mantle and play a key role in dictating arc processes including the long-term distribution of volcanic and seismic hazard.

Appendix A: Project Associates

A.1. VoiILA Group Consortium Members

Andreas Rietbrock[3], Saskia Goes[1], Jon Blundy[5,7], Nick Harmon[2], Catherine Rychert[2], Colin G. Macpherson[6], Jeroen Van Hunen[6], Mike Kendall[5,7], Jamie Wilkinson[1,8], Jon Davidson[6], Marjorie Wilson[9], George Cooper[5,13], Benjamin Maunder[1], Lidong Bie[4,14], Stephen Hicks[1], Richard Davy[1], Ben Chichester[2], Stephen Tait[10], Richie Robertson[11], Joan Latchman[11], and Frank Krüger[12]

[1]Department of Earth Sciences and Engineering, Imperial College London, UK

[2]Ocean and Earth Science, National Oceanography Centre Southampton, UK

[3]Geophysical Institute, Karlsruhe Institute of Technology, Karlsruhe, Germany

[4]Department of Earth Ocean & Ecological Sciences, University of Liverpool, UK

[5]School of Earth Sciences, University of Bristol, UK

[6]Department of Earth Sciences, Durham University, Durham, UK

[7]Department of Earth Sciences, University of Oxford, UK

[8]Department of Earth Sciences, Natural History Museum, London, UK

[9]School of Earth and Environment, University of Leeds, UK

[10]Institut de Physique du Globe de Paris, Jussieu, Paris, France

[11]Seismic Research Centre, The University of West Indies, Trinidad & Tobago

[12]Institute of Earth and Environmental Sciences, University of Potsdam, Germany

[13]School of Earth and Environmental Sciences, Cardiff University, UK

[14]School of Environmental Sciences, University of East Anglia, UK

References:

Allen, R. W., Collier, J. S., Stewart, A. G., Henstock, T., Goes, S., Rietbrock, A., & VoiLA_Team. (2019). The role of arc migration in the development of the Lesser Antilles: A new tectonic model for the Cenozoic evolution of the eastern Caribbean. *Geology, 47*(9), 891-895. https://doi.org/10.1130/G46708.1.

Anonymous. (1972). Penrose field conference on ophiolites. *Geotimes*(17(12)), 24-25.

Bangs, N. L. B., Westbrook, G. K., Ladd, J. W., & Buhl, P. (1990). Seismic Velocities from the Barbados Ridge Complex - Indicators of High Pore Fluid Pressures in an Accretionary Complex. *Journal of Geophysical Research-Solid Earth and Planets, 95*(B6), 8767-8782. https://doi.org/10.1029/Jb095ib06p08767.

Bie, L., Hicks, S., Rietbrock, A., Goes, S., Collier, J., Rychert, C., et al. (2022). Imaging slab-transported fluids and their deep dehydration from seismic velocity tomography in the Lesser Antilles subduction zone. *Earth and Planetary Science Letters, 586*, 117535. https://doi.org/10.1016/j.epsl.2022.117535.

Biju-Duval, B., Le Quellec, P., Mascle, A., Renard, V., & Valery, P. (1982). Multibeam bathymetric survey and high resolution seismic investigations on the Barbados Ridge complex (Eastern Caribbean): A key to the knowledge and interpretation of an accretionary wedge. *Tectonophysics, 86*(1-3), 275-304. https://doi.org/10.1016/0040-1951(82)90070-1.

Biju-Duval, B., Moore, J., & Shipboard Scientific Party. (1984). Site 543. Oceanic reference site east of the Barbados ridge complex. *Biju-Duval, B., and Moore, J. C, Init. Repts. DSDP A, 78*, 227-252.

Blanch, J. O., Robertsson, J. O., & Symes, W. W. (1993). Viscoelastic finite-difference modeling. In *SEG Technical Program Expanded Abstracts 1993* (pp. 990-993): Society of Exploration Geophysicists.

Braszus, B., Goes, S., Allen, R., Rietbrock, A., Collier, J., Harmon, N., et al. (2021). Subduction history of the Caribbean from upper-mantle seismic imaging and plate reconstruction. *Nat Commun, 12*(1), 4211. doi:10.1038/s41467-021-24413-0.

Cannat, M. (1993). Emplacement of mantle rocks in the seafloor at mid-ocean ridges. *Journal of Geophysical Research: Solid Earth, 98*(B3), 4163-4172. doi:10.1029/92jb02221.

Cannat, M., Mevel, C., Maia, M., Deplus, C., Durand, C., Gente, P., et al. (1995). Thin Crust, Ultramafic Exposures, and Rugged Faulting Patterns at Mid-Atlantic Ridge (22-Degrees 24-Degrees-N). *Geology, 23*(1), 49-52. https://doi.org/10.1130/0091-7613(1995)023<0049:Tcuear>2.3.Co;2.

Christeson, G. L., Bangs, N. L., & Shipley, T. H. (2003). Deep structure of an island arc backstop, Lesser Antilles subduction zone. *Journal of Geophysical Research-Solid Earth, 108*(B7). https://doi.org/10.1029/2002jb002243.

Christeson, G. L., Goff, J. A., & Reece, R. S. (2019). Synthesis of Oceanic Crustal Structure From Two-Dimensional Seismic Profiles. *Reviews of Geophysics, 57*(2), 504-529. doi:10.1029/2019rg000641.

Collier, J. S. (2017). *VoiLA - Volatile recycling in the Lesser Antilles arc: RRS James Cook cruise report JC149*. Retrieved from Imperial College London: https://www.bodc.ac.uk/resources/inventories/cruise_inventory/reports/jc149.pdf

Contreras-Reyes, E., Grevemeyer, I., Flueh, E. R., & Reichert, C. (2008). Upper lithospheric structure of the subduction zone offshore of southern Arauco peninsula, Chile, at similar to 38 degrees S. *Journal of Geophysical Research-Solid Earth, 113*(B7). https://doi.org/10.1029/2007jb005569.

Contreras-Reyes, E., Grevemeyer, I., Flueh, E. R., Scherwath, M., & Heesemann, M. (2007). Alteration of the subducting oceanic lithosphere at the southern central Chile trench-outer rise. *Geochemistry Geophysics Geosystems, 8*. https://doi.org/10.1029/2007gc001632.

Cooper, G. F., Macpherson, C. G., Blundy, J. D., Maunder, B., Allen, R. W., Goes, S., et al. (2020). Variable water input controls evolution of the Lesser Antilles volcanic arc. *Nature, 582*(7813), 525-529. doi:10.1038/s41586-020-2407-5.

Crameri, F., Shephard, G. E., & Heron, P. J. (2020). The misuse of colour in science communication. *Nature Communications, 11*(1), 5444. doi:10.1038/s41467-020-19160-7.

Dannowski, A., Grevemeyer, I., Ranero, C. R., Ceuleneer, G., Maia, M., Morgan, J. P., & Gente, P. (2010). Seismic structure of an oceanic core complex at the Mid-Atlantic Ridge, 22°19'N. *Journal of Geophysical Research, 115*(B7). doi:10.1029/2009jb006943.

Davy, R. G., Collier, J. S., Henstock, T. J., & the VoiLA Consortium. (2020). Wide-Angle Seismic Imaging of Two Modes of Crustal Accretion in Mature Atlantic Ocean Crust. *Journal of Geophysical Research-Solid Earth, 125*(6), e2019JB019100. doi:10.1029/2019JB019100.

Escartin, J., Smith, D. K., Cann, J., Schouten, H., Langmuir, C. H., & Escrig, S. (2008). Central role of detachment faults in accretion of slow-spreading oceanic lithosphere. *Nature, 455*(7214), 790-794. https://doi.org/10.1038/nature07333.

Evain, M., Galve, A., Charvis, P., Laigle, M., Kopp, H., Becel, A., et al. (2013). Structure of the Lesser Antilles subduction forearc and backstop from 3D seismic refraction tomography. *Tectonophysics, 603*, 55-67. https://doi.org/10.1016/j.tecto.2011.09.021.

Fujie, G., Kodaira, S., Kaiho, Y., Yamamoto, Y., Takahashi, T., Miura, S., & Yamada, T. (2018). Controlling factor of incoming plate hydration at the north-western Pacific margin. *Nat Commun, 9*(1), 3844. doi:10.1038/s41467-018-06320-z.

Fujiwara, T., Lin, J., Matsumoto, T., Kelemen, P. B., Tucholke, B. E., & Casey, J. F. (2003). Crustal evolution of the Mid-Atlantic Ridge near the Fifteen-Twenty Fracture Zone in the last 5 Ma. *Geochemistry Geophysics Geosystems, 4*(3). doi:10.1029/2002gc000364.

Gerya, T. V., Bercovici, D., & Becker, T. W. (2021). Dynamic slab segmentation due to brittle–ductile damage in the outer rise. *Nature, 599*(7884), 245-250. doi:10.1038/s41586-021-03937-x.

Goes, S., Collier, J., Blundy, J., Davidson, J., Harmon, N., Henstock, T., et al. (2019). Project VoiLA: Volatile Recycling in the Lesser Antilles. *Eos, 100*. https://doi.org/10.1029/2019eo117309.

Goff, J. A. (1991). A Global and Regional Stochastic-Analysis of near-Ridge Abyssal Hill Morphology. *Journal of Geophysical Research-Solid Earth, 96*(B13), 21713-21737. doi:10.1029/91jb02275.

Goff, J. A., Malinverno, A., Fornari, D. J., & Cochran, J. R. (1993). Abyssal Hill Segmentation: Quantitative analysis of the East Pacific Rise flanks 7°S-9°S. *Journal of Geophysical Research: Solid Earth, 98*(B8), 13851-13862. doi:10.1029/93jb01095.

Goff, J. A., Tucholke, B. E., Lin, J., Jaroslow, G. E., & Kleinrock, M. C. (1995). Quantitative-Analysis of Abyssal Hills in the Atlantic-Ocean - a Correlation between Inferred Crustal Thickness and Extensional Faulting. *Journal of Geophysical Research-Solid Earth, 100*(B11), 22509-22522. doi:10.1029/95jb02510.

Gregory, E. P. M., Singh, S. C., Marjanovic, M., & Wang, Z. K. (2021). Serpentinized peridotite versus thick mafic crust at the Romanche oceanic transform fault. *Geology, 49*(9), 1132-1136. doi:10.1130/G49097.1.

Grevemeyer, I., Ranero, C. R., & Ivandic, M. (2018). Structure of oceanic crust and serpentinization at subduction trenches. *Geosphere, 14*(2), 395-418. https://doi.org/10.1130/GES01537.1.

Growe, K., Grevemeyer, I., Singh, S. C., Marjanovic, M., Gregory, E. P. M., Papenberg, C., et al. (2021). Seismic Structure of the St. Paul Fracture Zone and Late Cretaceous to Mid Eocene Oceanic Crust in the Equatorial Atlantic Ocean Near 18 degrees W. *Journal of Geophysical Research-Solid Earth, 126*(11). 10.1029/2021jb022456.

Hacker, B. R. (2008). H2O subduction beyond arcs. *Geochemistry Geophysics Geosystems, 9*, 24. https://doi.org/10.1029/2007gc001707.

Hacker, B. R., Abers, G. A., & Peacock, S. M. (2003). Subduction factory - 1. Theoretical mineralogy, densities, seismic wave speeds, and H2O contents. *Journal of Geophysical Research-Solid Earth, 108*(B1). https://doi.org/10.1029/2001JB001127.

Ivandic, M., Grevemeyer, I., Berhorst, A., Flueh, E. R., & McIntosh, K. (2008). Impact of bending related faulting on the seismic properties of the incoming oceanic plate offshore of Nicaragua. *Journal of Geophysical Research-Solid Earth, 113*(B5). https://doi.org/10.1029/2007jb005291.

Kirby, S., Engdahl, R. E., & Denlinger, R. (1996). Intermediate-Depth Intraslab Earthquakes and Arc Volcanism as Physical Expressions of Crustal and Uppermost Mantle Metamorphism in Subducting Slabs. In D. W. S. G.E. Bebout, S.H. Kirby and J.P. Platt (Ed.), *Subduction Top to Bottom* (pp. 195-214): American Geophysical Union.

Kopp, H., Weinzierl, W., Becel, A., Charvis, P., Evain, M., Flueh, E. R., et al. (2011). Deep structure of the central Lesser Antilles Island Arc: Relevance for the formation of continental crust. *Earth and Planetary Science Letters, 304*(1-2), 121-134. https://doi.org/10.1016/j.epsl.2011.01.024.

Korenaga, J., Holbrook, W. S., Kent, G. M., Kelemen, P. B., Detrick, R. S., Larsen, H. C., et al. (2000). Crustal structure of the southeast Greenland margin from joint refraction and reflection seismic tomography. *Journal of Geophysical Research-Solid Earth, 105*(B9), 21591-21614. https://doi.org/10.1029/2000jb900188.

Laigle, M., Becel, A., de Voogd, B., Sachpazi, M., Bayrakci, G., Lebrun, J. F., et al. (2013). Along-arc segmentation and interaction of subducting ridges with the Lesser Antilles Subduction forearc crust revealed by MCS imaging. *Tectonophysics, 603*, 32-54. 10.1016/j.tecto.2013.05.028.

Laurencin, M., Graindorge, D., Klingelhoefer, F., Marcaillou, B., & Evain, M. (2018). Influence of increasing convergence obliquity and shallow slab geometry onto tectonic deformation and seismogenic behavior along the Northern Lesser Antilles zone. *Earth and Planetary Science Letters, 492*, 59-72. https://doi.org/10.1016/j.epsl.2018.03.048.

Lin, J., & Phipps-Morgan, J. (1992). The spreading rate dependence of three-dimensional mid-ocean ridge gravity structure. *Geophysical Research Letters, 19*(1), 13-16. 10.1029/91gl03041.

Lin, J., Purdy, G. M., Schouten, H., Sempere, J. C., & Zervas, C. (1990). Evidence from gravity data for focusedmagmatic accretionalong the Mid-Atlantic Ridge. *Nature, 344*(6267), 627-632. doi:10.1038/344627a0.

Macario, A., Haxby, W. F., Goff, J. A., Ryan, W. B. F., Cande, S. C., & Raymond, C. A. (1994). Flow line variations in abyssal hill morphology for the Pacific-Antarctic Ridge at 65°S. *Journal of Geophysical Research: Solid Earth, 99*(B9), 17921-17934. doi:10.1029/94jb01409.

Manea, V. C., Leeman, W. P., Gerya, T., Manea, M., & Zhu, G. (2014). Subduction of fracture zones controls mantle melting and geochemical signature above slabs. *Nat Commun, 5*(1), 5095. doi:10.1038/ncomms6095.

Marcaillou, B., Klingelhoefer, F., Laurencin, M., Lebrun, J. F., Laigle, M., Lallemand, S., et al. (2021). Pervasive detachment faults within the slow spreading oceanic crust at the poorly coupled Antilles subduction zone. *Communications Earth & Environment, 2*(1), 203. 10.1038/s43247-021-00269-6.

Marjanović, M., Singh, S. C., Gregory, E. P. M., Grevemeyer, I., Growe, K., Wang, Z., et al. (2020). Seismic Crustal Structure and Morphotectonic Features Associated With the Chain Fracture Zone and Their Role in the Evolution of the Equatorial Atlantic Region. *Journal of Geophysical Research: Solid Earth, 125*(10), e2020JB020275. https://doi.org/10.1029/2020JB020275.

Minshull, T. A., Muller, M. R., Robinson, C. J., White, R. S., & Bickle, M. J. (1998). Is the oceanic Moho a serpentinization front? *Geological Society, London, Special Publications, 148*(1), 71-80. doi:10.1144/gsl.Sp.1998.148.01.05.

Moore, J. C., Klaus, A., Bangs, N. L., Bekins, B., Bucker, C. J., Bruckmann, W., et al. (1998). Consolidation patterns during initiation and evolution of a plate-boundary decollement zone: Northern Barbados accretionary prism. *Geology, 26*(9), 811-814. https://doi.org/10.1130/0091-7613(1998)026<0811:CPDIAE>2.3.CO;2.

Naif, S., Key, K., Constable, S., & Evans, R. L. (2015). Water-rich bending faults at the Middle America Trench. *Geochemistry Geophysics Geosystems, 16*(8), 2582-2597. doi:10.1002/2015gc005927.

Patriat, M., Pichot, T., Westbrook, G. K., Umber, M., Deville, E., Benard, F., et al. (2011). Evidence for Quaternary convergence across the North America-South America plate boundary zone, east of the Lesser Antilles. *Geology, 39*(10), 979-982. https://doi.org/10.1130/G32474.1.

Paulatto, M., Laigle, M., Galve, A., Charvis, P., Sapin, M., Bayrakci, G., et al. (2017). Dehydration of subducting slow-spread oceanic lithosphere in the Lesser Antilles. *Nat Commun, 8*, 15980. doi:10.1038/ncomms15980.

Peacock, S. A. (1990). Fluid Processes in Subduction Zones. *Science, 248*(4953), 329-337. doi:10.1126/science.248.4953.329.

Peacock, S. M. (2001). Are the lower planes of double seismic zones caused by serpentine dehydration in subducting oceanic mantle? *Geology, 29*(4), 299-302. doi:10.1130/0091-7613(2001)029<0299:Atlpod>2.0.Co;2.

Pichot, T., Patriat, M., Westbrook, G. K., Nalpas, T., Gutscher, M. A., Roest, W. R., et al. (2012). The Cenozoic tectonostratigraphic evolution of the Barracuda Ridge and Tiburon Rise, at the western end of the North America-South America plate boundary zone. *Marine Geology, 303*, 154-171. https://doi.org/10.1016/j.margeo.2012.02.001.

Planert, L., Flueh, E. R., Tilmann, F., Grevemeyer, I., & Reston, T. J. (2010). Crustal structure of a rifted oceanic core complex and its conjugate side at the MAR at 5 degrees S: implications for melt extraction during detachment faulting and core complex formation. *Geophysical Journal International, 181*(1), 113-126. https://doi.org/10.1111/j.1365-246X.2010.04504.x.

Ranero, C. R., Morgan, J. P., McIntosh, K., & Reichert, C. (2003). Bending-related faulting and mantle serpentinization at the Middle America trench. *Nature, 425*(6956), 367-373. doi:10.1038/nature01961.

Robertsson, J. O. A., Blanch, J. O., & Symes, W. W. (1994). Viscoelastic finite-difference modeling. *Geophysics, 59*(9), 1444-1456. doi:10.1190/1.1443701.

Roth, S., Granot, R., & Downey, N. J. (2019). Discrete characterization of abyssal hills: Unraveling temporal variations in crustal accretion processes at the 10°30'N segment, East Pacific Rise. *Earth and Planetary Science Letters, 525*, 115762. https://doi.org/10.1016/j.epsl.2019.115762.

Sandwell, D. T., Muller, R. D., Smith, W. H., Garcia, E., & Francis, R. (2014). Marine geophysics. New global marine gravity model from CryoSat-2 and Jason-1 reveals buried tectonic structure. *Science, 346*(6205), 65-67. doi:10.1126/science.1258213.

Schlaphorst, D., Kendall, J. M., Collier, J. S., Verdon, J. P., Blundy, J., Baptie, B., et al. (2016). Water, oceanic fracture zones and the lubrication of subducting plate boundaries-insights from seismicity. *Geophysical Journal International, 204*(3), 1405-1420. https://doi.org/10.1093/gji/ggv509.

Schmidt, M. W., & Poli, S. (1998). Experimentally based water budgets for dehydrating slabs and consequences for arc magma generation. *Earth and Planetary Science Letters, 163*(1-4), 361-379. https://doi.org/10.1016/S0012-821X(98)00142-3.

Shillington, D. J., Becel, A., Nedimovic, M. R., Kuehn, H., Webb, S. C., Abers, G. A., et al. (2015). Link between plate fabric, hydration and subduction zone seismicity in Alaska. *Nature Geoscience, 8*(12), 961-U998. https://doi.org/10.1038/NGEO2586.

Shipley, T. H., Moore, G. F., Bangs, N. L., Moore, J. C., & Stoffa, P. L. (1994). Seismically Inferred Dilatancy Distribution, Northern Barbados Ridge Decollement - Implications for Fluid Migration and Fault Strength. *Geology, 22*(5), 411-414. https://doi.org/10.1130/0091-7613(1994)022<0411:Siddnb>2.3.Co;2.

Sleep, N. H., & Barth, G. A. (1997). The nature of oceanic lower crust and shallow mantle emplaced at low spreading rates. *Tectonophysics, 279*(1-4), 181-191. doi:10.1016/S0040-1951(97)00121-2.

Smith, D. K., Escartin, J., Schouten, H., & Cann, J. R. (2008). Fault rotation and core complex formation: Significant processes in seafloor formation at slow-spreading mid-ocean ridges (Mid-Atlantic Ridge, 13 degrees-15 degrees N). *Geochemistry Geophysics Geosystems, 9*. https://doi.org/10.1029/2007gc001699.

Tsuji, Y., Nakajima, J., & Hasegawa, A. (2008). Tomographic evidence for hydrated oceanic crust of the Pacific slab beneath northeastern Japan: Implications for water transportation in subduction zones. *Geophysical Research Letters, 35*(14). doi:10.1029/2008gl034461.

Tucholke, B. E., & Lin, J. (1994). A Geological Model for the Structure of Ridge Segments in Slow-Spreading Ocean Crust. *Journal of Geophysical Research-Solid Earth, 99*(B6), 11937-11958. doi:10.1029/94jb00338.

Vaddineni, V. A., Singh, S. C., Grevemeyer, I., Audhkhasi, P., & Papenberg, C. (2021). Evolution of the Crustal and Upper Mantle Seismic Structure From 0–27 Ma in the Equatorial Atlantic Ocean at 2° 43'S. *Journal of Geophysical Research: Solid Earth, 126*(6), e2020JB021390. doi:10.1029/2020JB021390.

Van Avendonk, H. J. A., Holbrook, W. S., Lizarralde, D., & Denyer, P. (2011). Structure and serpentinization of the subducting Cocos plate offshore Nicaragua and Costa Rica. *Geochemistry, Geophysics, Geosystems, 12*(6). doi:10.1029/2011gc003592.

van Keken, P. E., Hacker, B. R., Syracuse, E. M., & Abers, G. A. (2011). Subduction factory: 4. Depth-dependent flux of H2O from subducting slabs worldwide. *Journal of Geophysical Research, 116*(B1). doi:10.1029/2010jb007922.

Wan, K. Y., Lin, J., Xia, S. H., Sun, J. L., Xu, M., Yang, H. F., et al. (2019). Deep Seismic Structure Across the Southernmost Mariana Trench: Implications for Arc Rifting and Plate Hydration. *Journal of Geophysical Research-Solid Earth, 124*(5), 4710-4727. https://doi.org/10.1029/2018JB017080.

Wang, T., Tucholke, B. E., & Lin, J. (2015). Spatial and temporal variations in crustal production at the Mid-Atlantic Ridge, 25°N-27°30'N and 0-27 Ma. *Journal of Geophysical Research: Solid Earth, 120*(4), 2119-2142. doi:10.1002/2014jb011501.

Wessel, P., Matthews, K. J., Muller, R. D., Mazzoni, A., Whittaker, J. M., Myhill, R., & Chandler, M. T. (2015). Semiautomatic fracture zone tracking. *Geochemistry Geophysics Geosystems, 16*(7), 2462-2472. doi:10.1002/2015gc005853.

Westbrook, G. K. (1982). The Barbados Ridge Complex: tectonics of a mature forearc system. *Geological Society, London, Special Publications, 10*(1), 275-290. https://doi.org/10.1144/gsl.sp.1982.010.01.18.

White, R. S., Eccles, J. D., & Roberts, A. W. (2010). Constraints on volcanism, igneous intrusion and stretching on the Rockall–Faroe continental margin. *Geological Society, London, Petroleum Geology Conference series, 7*(1), 831-842. doi:10.1144/0070831.

White, R. S., Mckenzie, D., & Onions, R. K. (1992). Oceanic Crustal Thickness from Seismic Measurements and Rare-Earth Element Inversions. *Journal of Geophysical Research-Solid Earth, 97*(B13), 19683-19715. doi:10.1029/92jb01749.

Yamasaki, T., & Seno, T. (2003). Double seismic zone and dehydration embrittlement of the subducting slab. *Journal of Geophysical Research: Solid Earth, 108*(B4). doi:10.1029/2002JB001918.

Zelt, C. A., & Smith, R. B. (1992). Seismic Traveltime Inversion for 2-D Crustal Velocity Structure. *Geophysical Journal International, 108*(1), 16-34. https://doi.org/10.1111/j.1365-246X.1992.tb00836.x.

Bangs, N. L. B., T. H. Shipley, J. C. Moore and G. F. Moore (1999). "Fluid accumulation and channeling along the northern Barbados Ridge decollement thrust." Journal of Geophysical Research-Solid Earth 104: 20399-20414.

Minshull, T.A., Sinha, M.C., and Peirce, C. 2005. Multi-disciplinary, sub-seabed geophysical imaging. Sea Technology, 46(10), 27–31. URL: https://eprints.soton.ac.uk/18172/